

UniHOI: Learning Fast, Dense and Generalizable 4D Reconstruction for Egocentric Hand Object Interaction Videos

Chengbo Yuan¹, Geng Chen^{2,3†}, Li Yi^{1,2,3}, Yang Gao^{1,2,3‡}

¹Institute for Interdisciplinary Information Sciences, Tsinghua University

²Shanghai Artificial Intelligence Laboratory

³Shanghai Qi Zhi Institute

ycb24@mails.tsinghua.edu.cn gec001@ucsd.edu

{ericysi, gaoyangiiis}@mail.tsinghua.edu.cn

Abstract

Egocentric Hand Object Interaction (HOI) videos provide valuable insights into human interactions with the physical world, attracting growing interest from the computer vision and robotics communities. A key task in fully understanding the geometry and dynamics of HOI scenes is dense pointclouds sequence reconstruction. However, the inherent motion of both hands and the camera makes this challenging. Current methods often rely on time-consuming test-time optimization, making them impractical for reconstructing internet-scale videos. To address this, we introduce **UniHOI**, a model that unifies the estimation of all variables necessary for dense 4D reconstruction, including camera intrinsic, camera poses, and video depth, for egocentric HOI scene in a fast feed-forward manner. We end-to-end optimize all these variables to improve their consistency in 3D space. Furthermore, our model could be **trained solely on large-scale monocular video datasets**, overcoming the limitation of scarce labeled HOI data. We evaluate UniHOI with both in-domain and zero-shot generalization setting, surpassing all baselines in pointclouds sequence reconstruction and long-term 3D scene flow recovery. UniHOI is the first approach to offer **fast, dense, and generalizable monocular egocentric HOI scene reconstruction in the presence of motion**. Code and trained model will be released in the future.

1. Introduction

Egocentric Hand Object Interaction (HOI) videos capture a vast amount of knowledge about human interaction with the physical world, particularly in tool usage. Due to this rich

[†] Work done during the internship at Shanghai AI Lab and Qi Zhi Institute. [‡] Corresponding authors.

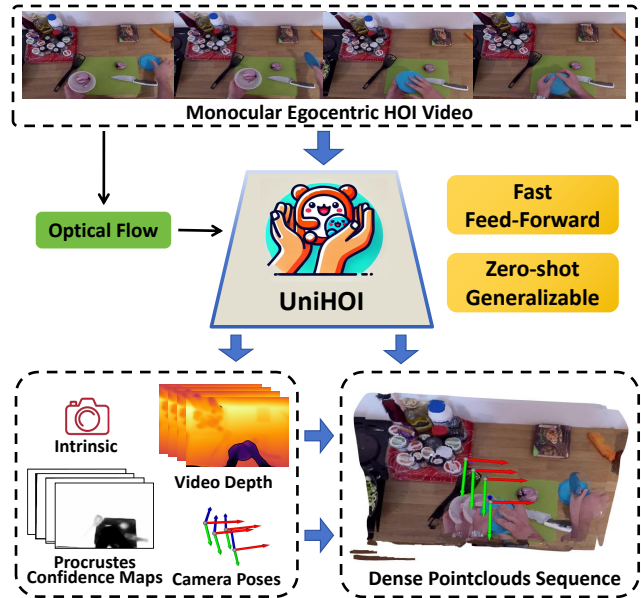


Figure 1. We propose UniHOI, a generalizable model that unifies camera intrinsic, procrustes-alignment confidence maps (for camera poses estimation), camera poses, and video depth estimation for fast and dense 4D reconstruction of egocentric HOI scene.

source of interaction knowledge, egocentric human videos have gained increasing interest from both the research community (e.g., computer vision [51, 91] and robotics [44, 87]) and industry (e.g., virtual reality [47]).

To better understand the geometry and dynamics in these activities, a crucial task is the dense 4D reconstruction from internet-scale egocentric HOI video datasets [15, 21]. Here, dense 4D reconstruction is represented as a **pointclouds sequence which captures the 3D position of every pixel in each frame within a global coordinate system** [77, 90], preserving maximal geometry details. This task requires:

(1) fast processing speeds to support large-scale reconstruction, (2) dense per-pixel reconstruction, (3) strong generalization to adapt to unseen HOI scenes, and (4) the ability to handle dynamic motions in HOI videos. However, current methods do not meet these demands. Traditional methods [57, 70], such as Structure-from-Motion (SfM) or SLAM system combined with dense depth estimation [49, 86], face significant challenges in reconstructing dynamic scenes. These multi-step approaches also suffer from accumulated errors and inconsistencies between modules [74, 77]. Recent methods have focused on time-consuming test-time optimization techniques [29, 32, 40, 89], like Gaussian Splatting [26], but their speed is impractical for reconstructing large-scale egocentric datasets [21, 38].

To address these challenges, we aim to explore fast, dense and generalizable reconstruction of highly dynamic egocentric HOI scenes. Our key insight is to simultaneously predict all variables necessary for dense 4D reconstruction with a unified model (Figure 1), including camera intrinsic, camera poses and video depth [37, 64]. This paradigm enables fast, streaming feed-forward inference, achieving speeds 30x faster than the current test-time optimization methods [68, 75, 88]. We optimize the prediction of all variables together by directly supervising the reconstructed pointclouds sequence in 3D space. This end-to-end optimization enhances **scale and geometry consistency** across all variables, mitigating the accumulated errors and inconsistencies in previous multi-step methods, resulting in improved reconstruction outcomes [77].

One challenge in training HOI scene reconstruction model is the limited availability of datasets with pointclouds sequence labels [31, 76]. To overcome this, we train our model purely on large-scale monocular video datasets by leveraging priors from foundation vision models. Specifically, we (1) regularize the pointclouds sequence with pre-computed per-frame monocular scene reconstruction results [49]; (2) ensure inter-frame consistency via 3D flow [83] and tracking [24] with a designed scale-agnostic loss. We transform camera pose estimation into a dense procrustes-alignment confidence map prediction problem [63, 64] and further (3) regularize the confidence map with predicted HOI masks from off-the-shelf model [91]. By training on large-scale, unlabeled mixed datasets [15, 20, 31, 34, 38], our model achieves zero-shot generalization ability.

We evaluate our model on both in-domain and zero-shot unseen scenes. UniHOI successfully recovers the 3D structure of scenes and the motion of dynamic parts, even in challenging synthetic surgery HOI videos [76]. We also perform a quantitative comparison of our model with other methods that have near-linear time complexity (to the number of frames), focusing on two fundamental 4D tasks: dense pointclouds sequence reconstruction [64, 77] and long-term 3D scene flow recovery [3, 30, 87]. UniHOI demonstrates

strong performance on evaluation metrics and outperforms all other baseline methods.

In conclusion, our main contributions are as follows:

- We propose UniHOI, a model that unifies camera intrinsic, camera poses and video depth estimation for fast, dense and generalizable 4D reconstruction of egocentric HOI scene.
- We train our model solely on large-scale, unlabeled monocular HOI datasets, which helps alleviate the issue of labeled data scarcity.
- UniHOI demonstrates promising performance in both in-domain and zero-shot unseen scenes, surpassing all baselines in pointclouds sequence reconstruction and long-term 3D scene flow recovery tasks.

2. Related Works

2.1. Monocular Depth Estimation

Monocular depth estimation has made significant progress in recent years [54]. Supervised learning models have shown strong generalization capabilities [4, 6, 23, 49, 79, 84, 86]. Our work builds on UniDepth [49], a state-of-the-art model that unifies camera intrinsic and depth estimation for single image. Another line of works focus on unsupervised training [5, 37, 62, 69, 85]. These methods train depth estimators purely on monocular videos using photometric error supervision [65, 66], often by leveraging camera labels or learning camera predictors. Despite recent progress, no methods have yet demonstrated strong generalization across both camera and depth. Our approach also unifies depth and camera prediction and trained solely on monocular video datasets [15]. However, our primary focus is on generalizable 4D reconstruction for egocentric HOI scenes, requiring zero-shot prediction for both depth and camera.

2.2. Structure from Motion and SLAM Systems

Structure from Motion (SfM) [14, 57, 58, 94] and monocular (dense) visual SLAM systems [7, 43, 55, 70, 92] aim to reconstruct 3D structures and estimate camera poses from image sequences. These methods often struggle with dynamic scenes which pose ill condition for the epipolar constraint [77]. Moreover, most of them typically can not provide dense pixel-level reconstructions for all frames. One solution is to combine visual odometry [1, 8, 70, 78] with dense depth estimation [49, 86] (to constrain the geometry of dynamic parts). However, these multi-step approaches are prone to accumulated errors and inconsistencies between modules. Recently, FlowMap [64] proposes an end-to-end differentiable (static scene) SfM, optimizing feed-forward estimators of depths, poses, and intrinsic simultaneously. We adopt its key ideas and extend it to a generalizable version for dynamic HOI scenes.

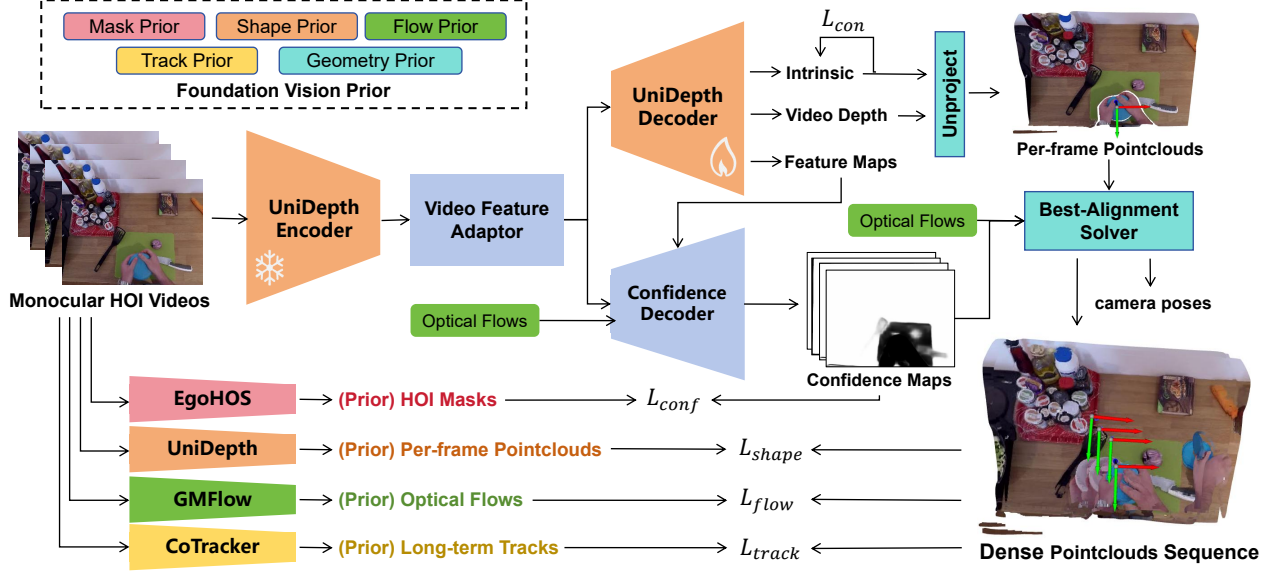


Figure 2. The overview of our UniHOI framework. The model first simultaneously predicts camera intrinsic, video depth, and procrustes-alignment confidence maps (for camera pose estimation). Camera poses are then calculated by aligning unprojected pointclouds from different frames with predicted confidence maps. The final dense pointclouds sequence reconstruction is assembled using all the predicted variables. We train our model purely on unlabeled HOI video datasets, leveraging foundation vision priors from pretrained EgoHOS [91], UniDepth [49], GMFlow [83], and CoTracker [24] as training supervision.

2.3. Dense 4D Reconstruction for Dynamic Scenes

Reconstructing 4D dynamic scenes remains an open challenge in the computer vision community. Some works [12, 29, 32, 40, 68, 75, 88, 89, 93] first compute vision cues (e.g., camera pose, depth, optical flow) and then perform per-scene test-time optimization. While these approaches yield high-quality results, they are time-consuming and impractical for large-scale reconstructions [30]. Alternatively, some methods [25, 90] attempt fast, feed-forward 4D reconstruction. Concurrent with our work, MonSt3R [90] finetunes the end-to-end Multi-View Stereo (MVS) model DUST3R [33, 77] on simulated labeled dynamic scene images [95] to enhance its ability to handle dynamics. However, such data is scarce in the HOI field. In contrast, our method relies solely on large-scale unlabeled videos for training [15].

2.4. HOI Scene Understanding and Reconstruction

Egocentric HOI videos and datasets [15, 18, 20, 21, 31, 34, 38, 47, 76] contain extensive interactions between human hands and the physical world. This interaction knowledge are crucial for applications in robotics [2, 44, 81, 87], virtual reality [47], and intelligent agents [42, 80]. To better understand these dynamic interactions, tasks such as detection [60], segmentation [91], intention recognition [34, 52], motion prediction [3, 53], and hand-object reconstruction [48, 50] have been applied to HOI videos. However, dense reconstruction of entire HOI scenes remains an open prob-

lem. EgoGaussian [89] addresses this with time-intensive test-time optimization through Gaussian Splatting [26]. Our approach, on the other hand, explores this problem with a fast ($> 30x$ speedup), feed-forward, and scalable pathway.

3. Preliminary

3.1. Problem Definition

A monocular egocentric HOI video can be represented as a sequence of frames $\{I_t \in R^{H \times W \times 3}\}$, where $t = 0, 1, \dots, T-1$ and T is the total number of frames. Each frame is a RGB image with a resolution of $H \times W$. Given a video, our goal is to estimate a sequence of dense pointclouds, $\{\hat{S}_t \in R^{H \times W \times 3}\}$, which capture the 3D position of every pixel in each frame within a global coordinate system. To achieve this, we decompose the pointclouds sequence into: (1) video depth $\{\hat{D}_t \in R^{H \times W}\}$; (2) camera intrinsic $\hat{K} \in R^{3 \times 3}$ for unprojecting depth into per-frame pointclouds; and (3) camera poses $\{\hat{P}_t \in R^{4 \times 4}\}$ in camera-to-world format for projecting the per-frame pointclouds into global coordinates. Then the pointclouds sequence $\{\hat{S}_t\}$ could be calculated as:

$$\hat{X}_t = \hat{D}_t(i, j) \hat{K}^{-1} h(p(i, j)) \quad (1)$$

$$\hat{S}_t(i, j) = h^{-1}(\hat{P}_0^{-1} \hat{P}_t h(\hat{X}_t)) \quad (2)$$

where (i, j) refers to the pixel position $p(i, j)$, $\hat{X}_t \in R^{H \times W \times 3}$ represents the per-frame pointclouds, and $h(\cdot)$

is the homogeneous operator that adds an extra dimension with a value of 1 to the coordinate system.

3.2. Pose Estimation with Weighted Procrustes

Following FlowCam [63], we reframe camera poses estimation as a dense prediction problem to improve robustness and generalization. Specifically, we estimate camera poses using a weighted procrustes formulation. Given the estimated depth \hat{D}_t and camera intrinsic \hat{K} , we first unproject the depths into per-frame pointclouds \hat{X}_t . We then estimate the optical flow from frame i to frame j , denoted as $\hat{u}_{i,j}$. The pointclouds $\hat{X}_j^{\leftarrow i}$ of frame j , induced by optical flow $\hat{u}_{i,j}$, is defined as the interpolation of \hat{X}_j using $\hat{u}_{i,j}$. The unweighted procrustes-alignment aims to find a pose transformation that best aligns \hat{X}_i with $\hat{X}_j^{\leftarrow i}$.

Direct conducting procrustes-alignment may be fragile to (1) occlusions, (2) scene edges, (3) inaccurate optical flow, and (4) dynamic regions. To address these challenges, we additionally estimate a procrustes-alignment confidence map $\hat{\mathcal{M}}_{i,j} \in R^{H \times W}$ to filter out unreliable points. The final camera pose estimation is formulated as:

$$\hat{P}_{i,j} = \arg \min_{P \in SE(3)} \|\hat{\mathcal{M}}_{i,j}(\hat{X}_i - P\hat{X}_j^{\leftarrow i})\| \quad (3)$$

This can be solved in closed form using the singular value decomposition (SVD) [11], allowing a differentiable and learnable camera pose estimation process via gradient descent [64]. The confidence maps $\hat{\mathcal{M}}$ also help to correct inherent errors in the optical flow estimation network.

4. Methodology

Figure 2 summarizes the overall framework of our work. The key insight lies in utilizing a unified model to jointly predict camera intrinsic, camera poses, and video depth (Sections 3.1, 3.2), while optimizing their consistency through end-to-end supervision in 3D space. Our model is built on the UniDepth [49] backbone (Section 4.1). We train our model solely on monocular HOI videos, leveraging a mixture of large-scale unlabeled egocentric human video datasets. To accomplish this, we incorporate vision priors from pretrained vision models (Section 4.2). After training, the model enables dense dynamic scene reconstruction in a fast feed-forward manner (Section 4.3). We name our model **UniHOI**, as it Unifies depth and camera prediction for dynamic egocentric HOI scene reconstruction.

4.1. Model Architecture

Our model builds upon UniDepth [49], a universal estimator for predicting depth and camera intrinsics with encoder-decoder architecture. More details of model architecture could be found in Appendix B. Since UniDepth has been

pretrained on millions of depth images, showing strong generalization for scene reconstruction, we freeze its encoder to retain pretrained knowledge and only finetune its decoder.

We make several updates to the UniDepth backbone. First, we extend it from an image-based estimator to a multi-frame video version. Our model takes N_w images as input, extracting features separately using the encoder for each frame. We then use Unet3D-based [13] and Transformer-based [72] adaptors [9, 35] to fuse the features along the time dimension. These fused features are then fed into the UniDepth decoder to predict both depth and intrinsic for each frame, with intrinsic averaged across frames to determine the overall video intrinsic.

We also introduce a new decoder to predict the procrustes-alignment confidence maps $\hat{\mathcal{M}}$. For efficiency, we only estimate confidence maps and camera poses for pairs of nearby frames, resulting in $\hat{\mathcal{M}} \in R^{(T-1) \times H \times M}$. Camera poses are then estimated with weighted procrustes-alignment (Section 3.2).

4.2. Model Training with Foundation Vision Prior

Given the relatively small size of labeled egocentric HOI datasets [18, 31, 38, 76] compared to the larger unlabeled datasets [15, 20, 21, 34], we focus on training our model solely with unlabeled monocular videos. To accomplish this, we leverage foundational vision priors estimated from other models [24, 49, 83, 91]. We optimize all geometric variable prediction jointly by applying supervision directly on the pointclouds sequence. In the following, we introduce the supervision loss used in our framework.

3D Shape Prior Supervision After predicting the depth \hat{D}_t and camera intrinsic \hat{K} , we first recover per-frame pointclouds \hat{X}_t using Equation (1). We then regularize the shape of \hat{X}_t with the prediction \tilde{X}_t from UniDepth [49]:

$$\mathcal{L}_{shape} = \frac{1}{H \times W} \min_{s,R,T} \|sR\hat{X}_t + T - \tilde{X}_t\| \quad (4)$$

Here, (s, R, T) represents the scaled SE(3) transformation used for alignment, aiming to enable regularization on a relative scale [6]. The optimal transformation can be solved in closed form using SVD [11]. Note that \mathcal{L}_{shape} also helps **constrain dynamic parts of scenes** relative to static areas.

Pseudo Confidence Maps Supervision In UniHOI, camera poses are estimated using weighted procrustes-alignment based on predicted confidence maps. The confidence maps address several challenges in procrustes-alignment (Section 3.2), with dynamic areas and scene edges being two key factors. We regularize the model using pre-computed pseudo-maps $\hat{\mathcal{M}}$, which combine two sources: (1) Pseudo-dynamic areas: dynamic regions are regularized with a pre-computed HOI mask from EgoHOS

[91], as hand-object interactions are the main source of motion; (2) Pseudo-edges: sharp scene edges are approximated using flying pixels [56] derived from UniDepth [49] depth predictions.

$$\mathcal{L}_{maps} = BCELoss(\hat{\mathcal{M}}, \tilde{\mathcal{M}}) \quad (5)$$

For the Epic-Kitchen [15] dataset, we additionally estimate dynamic masks using epipolar loss [39] when hands are out of the camera view. See [39] for details.

3D Flow and Track Prior Supervision The loss term \mathcal{L}_{shape} regularizes per-scene results but cannot ensure scale and geometry consistency across frames. To resolve this, we align the scale and geometry of pointclouds between frames using optical flow [83] and long-term tracking [24]. This alignment minimizes the 3D reprojection error in high-confidence (static) regions between frames i and j in a **scale-agnostic** manner. Specifically, we use the predicted camera poses $\hat{P}_{i,j}$ derived from $\hat{M}_{i,j}$ to project the optical-flow-induced pointclouds $\hat{X}_j^{\leftarrow i}$ back into the coordinate system of frame i , and then compare the distance between this projection and the pointclouds \hat{X}_i of frame i :

$$\mathcal{L}_{flow/track} = \frac{\|\tilde{M}_{i,j}(\hat{X}_i - \hat{P}_{i,j}\hat{X}_j^{\leftarrow i})\|}{F(\hat{X}_i)\|\hat{M}_{i,j}\|} \quad (6)$$

where $F(\cdot)$ computes the first principal component of the pointclouds. We use $F(\hat{X}_i)$ as a proxy for the scale of \hat{X}_i and place it in the denominator of $\mathcal{L}_{flow/track}$ to prevent the pointclouds from collapsing to a single point. Compared to widely used photometric loss [64, 65], $\mathcal{L}_{flow/track}$ promotes more 3D consistency in the predictions.

Camera Consistency Self-Supervision We introduce a self-supervised loss \mathcal{L}_{con} to enhance the consistency of camera intrinsic predictions. For two frame sequences V_1 and V_2 from the same video clip, we enforce the intrinsic predictions to be as similar as possible:

$$\mathcal{L}_{con} = \|\hat{K}_{V_1} - \hat{K}_{V_2}\| \quad (7)$$

Final Loss Function The final loss is:

$$\mathcal{L} = \alpha\mathcal{L}_{shape} + \beta\mathcal{L}_{flow} + \gamma\mathcal{L}_{track} + \lambda\mathcal{L}_{maps} + \mu\mathcal{L}_{con} \quad (8)$$

where we set $\alpha = 4$, $\beta = \gamma = 5$, $\lambda = 1$, $\mu = 0.005$ as loss weights to balance each supervision.

4.3. Inference Strategy

Due to GPU memory limitations, only a limited number of frames can be processed in a single feed-forward prediction. However, we can predict videos with infinite frames in a stream manner using a sliding window. The video is first split into N_w frames sub-clips with N_o overlapping frames

Training	Frames	Camera Motion	Action	Scene
H2O	40K	Small	Simple	Clean
HOI4D	540K	Medium	Simple	Clean
FPHA	73K	Medium	Complex	Clutter
EgoPAT3D	823K	Large	Medium	Medium
Epic-Kitchen	9.7M	Large	Complex	Clutter
Evaluation	Frames	Setting	Label	Note
H2O	8K	In-domain	Calibration	Bi-manual
HOI4D	12K	In-domain	SfM	Contain Noise
ARCTIC-HOI	13K	Zero-shot	Mocap	Only HOI label
POV-Surgery	26K	Zero-shot	Synthesis	Unrealistic

Table 1. HOI video datasets we used for training and evaluation.

between neighbors. Then we predict neighboring windows independently. Let w_i represent the i -th sub-clip, E_i the timestamp set of w_i , and $\hat{S}^{w_i}, \hat{S}^{w_{i+1}}$ the predictions for two neighboring sub-clips. The latter is then then aligned and concatenated to the former as follows:

$$(s^*, R^*, T^*) = \arg \min_{s, R, T} \|sR\hat{S}_{E_{i+1}^{ov}}^{w_i} + T - \hat{S}_{E_{i+1}^{ov}}^{w_{i+1}}\| \quad (9)$$

$$\hat{S}^{[w_i, w_{i+1}]} = [\hat{S}^{w_i}, s^*R^*\hat{S}_{E_{i+1}^{ov}-E_{i+1}^{ov}}^{w_{i+1}} + T^*] \quad (10)$$

where E_{i+1}^{ov} represents the overlapping timestamps between w_i and w_{i+1} , and $[\cdot, \cdot]$ denotes the concatenation operator.

5. Experiments

5.1. Datasets

Table 1 presents the datasets used for training and evaluation. For more detailed information, please refer to Appendix A. Our model training utilizes a combination of ego-centric HOI videos selected from H2O[31], HOI4D[38], FPHA[20], EgoPAT3D[34], and Epic-Kitchen[15]. Each video is divided into 20-frame sub-clips for batch training. The total training data comprises 11.2 million frames, with the majority (9.7M frames) coming from the unlabeled Epic-Kitchen dataset.

For model evaluation, we use datasets with pointclouds sequence labels. For in-domain evaluation, we use H2O[31] and HOI4D[38]. We split the datasets based on Scene ID to ensure that the test set scenes are not included in the training set. For the zero-shot generalization setting, we use POV-Surgery[76] and ARCTIC[18] (only Mocap [71] HOI labels). To eliminate redundancy, we only use the first record of each task from the first participant. Videos are split into 40-frame sub-clips for batched evaluation. Note that ARCTIC only provides labels for hand and object. We rename it as ARCTIC-HOI to emphasize that it is primarily used to evaluate HOI part.

	HOI4D				H2O				POV-Surgery [†]				ARCTIC-HOI [†]			
	CD ↓	F ₁ ↑	F _{2.5} ↑	F ₅ ↑	CD ↓	F ₁ ↑	F _{2.5} ↑	F ₅ ↑	CD ↓	F ₁ ↑	F _{2.5} ↑	F ₅ ↑	CD ↓	F ₁ ↑	F _{2.5} ↑	F ₅ ↑
DS+UniDepth	<u>6.7</u>	<u>23.2</u>	<u>53.4</u>	<u>79.9</u>	<u>5.1</u>	36.5	75.0	93.2	<u>39.1</u>	7.7	20.0	38.7	<u>2.9</u>	<u>22.2</u>	60.2	<u>84.7</u>
MFVR+UniDepth	8.9	15.4	38.2	68.0	4.7	<u>47.8</u>	<u>81.5</u>	<u>94.2</u>	223.3	3.6	9.6	19.1	5.8	12.6	33.8	63.2
DUST3R	8.6	24.0	53.2	76.8	8.8	23.1	56.0	<u>82.7</u>	55.4	<u>9.7</u>	<u>24.7</u>	<u>45.1</u>	3.2	20.8	53.7	83.1
MonSt3R	7.6	21.4	50.8	77.9	14.7	15.1	42.4	70.0	94.5	6.5	17.8	34.8	5.4	9.9	31.8	65.0
UniHOI (Ours)	5.9	27.9	59.6	83.1	<u>5.1</u>	54.2	83.9	94.4	33.8	13.5	32.0	53.9	2.8	24.1	<u>57.5</u>	86.2

Table 2. The evaluation results for 4D pointclouds sequence reconstruction are presented, using 3D Chamfer Distance (CD, mm) and 3D Pointclouds F-score (F_δ, %). † indicates zero-shot generalization for UniHOI. For ARCTIC-HOI, the evaluation focuses specifically on the reconstruction quality of the hand-object region. On average, UniHOI demonstrates a clear advantage across the metrics.

	HOI4D				H2O				POV-Surgery [†]				ARCTIC-HOI [†]			
	ADE↓	FDE↓	P ₅ ↑	P ₁₀ ↑	ADE↓	FDE↓	P ₅ ↑	P ₁₀ ↑	ADE↓	FDE↓	P ₅ ↑	P ₁₀ ↑	ADE↓	FDE↓	P ₅ ↑	P ₁₀ ↑
DS+UniDepth	<u>64.0</u>	75.1	<u>54.0</u>	<u>82.5</u>	46.4	48.6	67.6	95.0	<u>168.9</u>	<u>199.7</u>	13.2	39.8	<u>53.9</u>	72.1	60.1	<u>86.8</u>
MFVR+UniDepth	88.8	94.8	23.1	69	<u>40.9</u>	<u>42.8</u>	<u>75.8</u>	97.0	504.5	767.6	3.2	13.6	102.0	154.6	33.8	62.0
DUST3R	79.2	75.8	47.7	75.1	71.7	71.5	54.3	75.9	412.8	407.2	<u>14.8</u>	<u>44.9</u>	214.3	181.6	52.2	82.3
MonSt3R	70.2	<u>71.0</u>	50.7	80.6	96.3	97.1	27.6	67.3	201.8	208.9	8.4	31.8	83.9	106.3	28.4	69.9
UniHOI (Ours)	57.3	60.6	59.2	87.0	37.0	38.9	77.0	<u>96.4</u>	125.0	138.9	19.1	55.2	53.8	72.1	<u>57.2</u>	87.3

Table 3. The evaluation results for long-term 3D scene flow recovery are presented, with ADE (mm), FDE (mm), and Precision (P_δ, %). † denotes zero-shot generalization for UniHOI. For ARCTIC-HOI, the evaluation focuses solely on hand-object recovery quality. Overall, UniHOI significantly outperforms the other baselines.

5.2. Implementation Details

We initialize our model with the pretrained UniDepthV2-L weights[49] and freeze the encoder. For input preprocessing, we resize the images to a resolution of 288 × 384. During training, each data point consists of 4 frames sampled from each sub-clip, with the interval between frames randomly selected from the range [1, 4]. We employ the Adam [27] optimizer with a learning rate of 5e-5 and a batch size of 16. The model is trained on 8 NVIDIA A800 GPUs for 350k iterations, requiring approximately 28 days to complete the training process.

For inference, we observe that the model remains robust regardless of the overlapping size N_o between neighbouring windows. To optimize inference speed, we set the overlap to 1 frame. For stability, we set window size $N_w = 4$ by default, the same with training process. We provide the ablation study of inference strategy in Appendix D. Running inference on a single NVIDIA GeForce RTX3090 GPU with a batch size of 1 achieves a speed of approximately 0.21 seconds per frame.

5.3. Baseline

We compare our model against previous methods that (1) provide dense 4D reconstruction, (2) have nearly linear time complexity (to the number of frames), supporting large-scale reconstruction, and (3) demonstrate zero-shot

(Only for HOI)	ADE↓	FDE↓	P ₅ ↑	P ₁₀ ↑
HOI4D	79.3 / 76.6	84.6 / 78.4	48.3 / 46.2	77.8 / 81.0
H2O	43.6 / 40.5	45.8 / 41.4	68.6 / 71.2	95.7 / 98.2
POV-Surgery [†]	196.0 / 192.2	213.4 / 206.4	9.9 / 9.9	32.4 / 32.8

Table 4. Additional long-term 3D scene flow results on the HOI part. Values are presented in the format ‘DS+UniDepth / UniHOI (Ours)’. Both models demonstrate comparable performance, with UniHOI showing a modest advantage.

generalization capability. **DS+UniDepth** (DROID-SLAM [70] + UniDepth [49]) combines depth estimation with learning-based RGBD visual odometry. **MFVR+UniDepth** (MapFreeVR [1] + UniDepth [49]) first estimates image depth, then computes camera poses with correspondence estimation (optical flow [83] in our setting) and procrustes solver. Additionally, we integrate HOI masks from EgoHOS[91] to filter out the HOI region for procrustes-alignment. This baseline could be viewed as a modularized version of UniHOI. **DUST3R** [77] supports end-to-end reconstruction. We use the “swin” mode from the original implementation to achieve $\mathcal{O}(T)$ inference. Lastly, **MonSt3R** [90] is a finetuned version of DUST3R on synthetic dynamic datasets, aimed at improving reconstruction performance in dynamic areas.

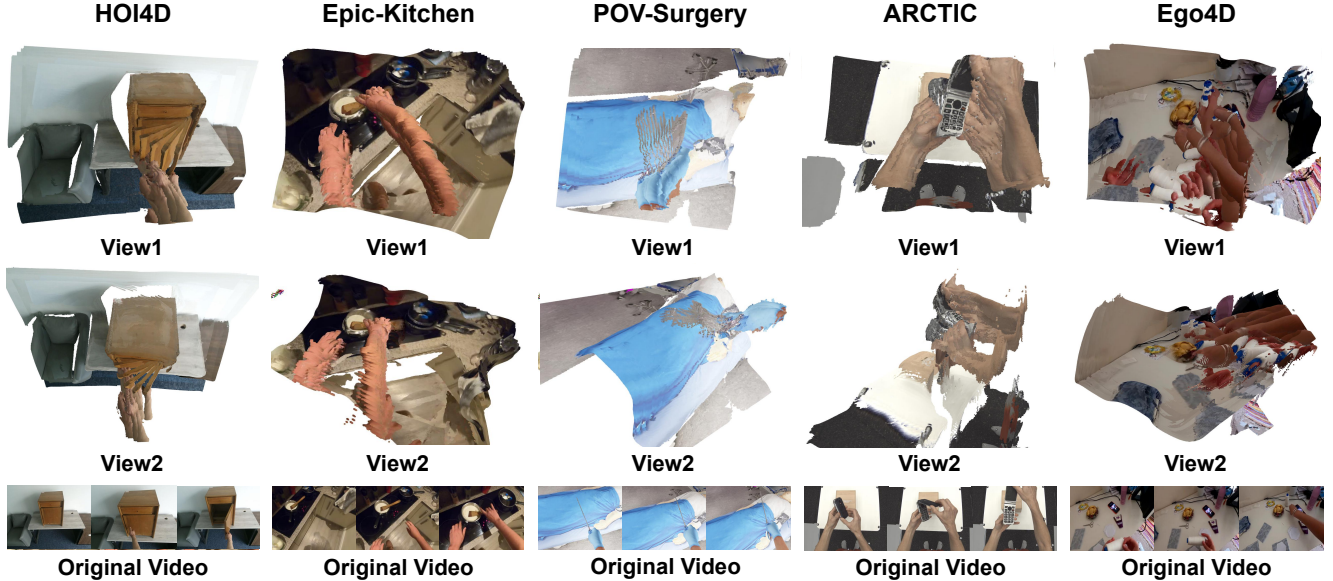


Figure 3. The visualization of the dense pointclouds sequence reconstruction of UniHOI. While some noise remains (e.g., non-overlapping edges of static parts), UniHOI effectively recovers the overall scene structure and the dynamic motion elements to a some extent. See Appendix H for more visualization. We provide qualitative comparison and visualization with baseline methods in Appendix I.

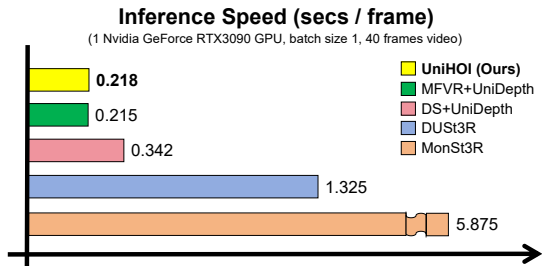


Figure 4. Inference speed comparison of different methods.

6. Result

Here we present the evaluation results of all methods on two fundamental 4D reconstruction tasks: dense pointclouds sequence reconstruction [64, 77, 90] and long-term 3D scene flow recovery [3, 30, 87]. Detailed definitions of all metrics can be found in Appendix C.

6.1. Dense Pointclouds Sequence Reconstruction

Task and Metric Dense pointclouds sequence reconstruction [64, 77] requires the model to reconstruct the $H \times W$ pointclouds of each frame within a global coordinate system. Since the scale of the pointclouds is ambiguous for monocular reconstruction, we first apply an estimated globally scaled $SE(3)$ transformation (s, R, T) to align the prediction to the ground-truth. We then evaluate the accuracy of each frame’s shape and average these results as the final evaluation score. Following [46, 49], we use the 3D Cham-

fer Distance (CD, mm) and the 3D Pointclouds F-score (F_δ , %) to assess shape similarity. We use the notation F_δ to denote the F-score with a threshold of δ centimeters (cm) as the positive criterion.

Results The quantitative evaluation results are presented in Table 2. UniHOI shows best performance among all methods. DS+UniDepth also shows good performance across many metrics. MFVR+UniDepth, the modularized version of our model, performs significantly worse than our model on most metrics. This underscores the importance of jointly optimizing all geometric variables with unified supervision in 3D space, reducing inconsistencies between the different modules. Due to the limited availability of labeled HOI data for training, DUS3R and MonSt3R shows limited performance on HOI scene. We also visualize the pointclouds sequence reconstruction in Figure 3. Although some noise remains (e.g., non-overlapping edges in static parts), it is evident that our model effectively recovers both the overall scene shape and the dynamic motion elements.

6.2. Long-term 3D Scene Flow Recovery

Task Long-term 3D scene flow [73] captures both the structure and dynamics of HOI scenes in a compact format, making it valuable for various applications such as perception [61], autonomous driving [41], and robot learning [17, 59, 87]. Given a video and a set of query points in the first frame, the 3D flow [30, 87] represents the future trajectory of each query point in 3D space. Since HOI datasets lack explicit 3D flow labels, we first employ Co-

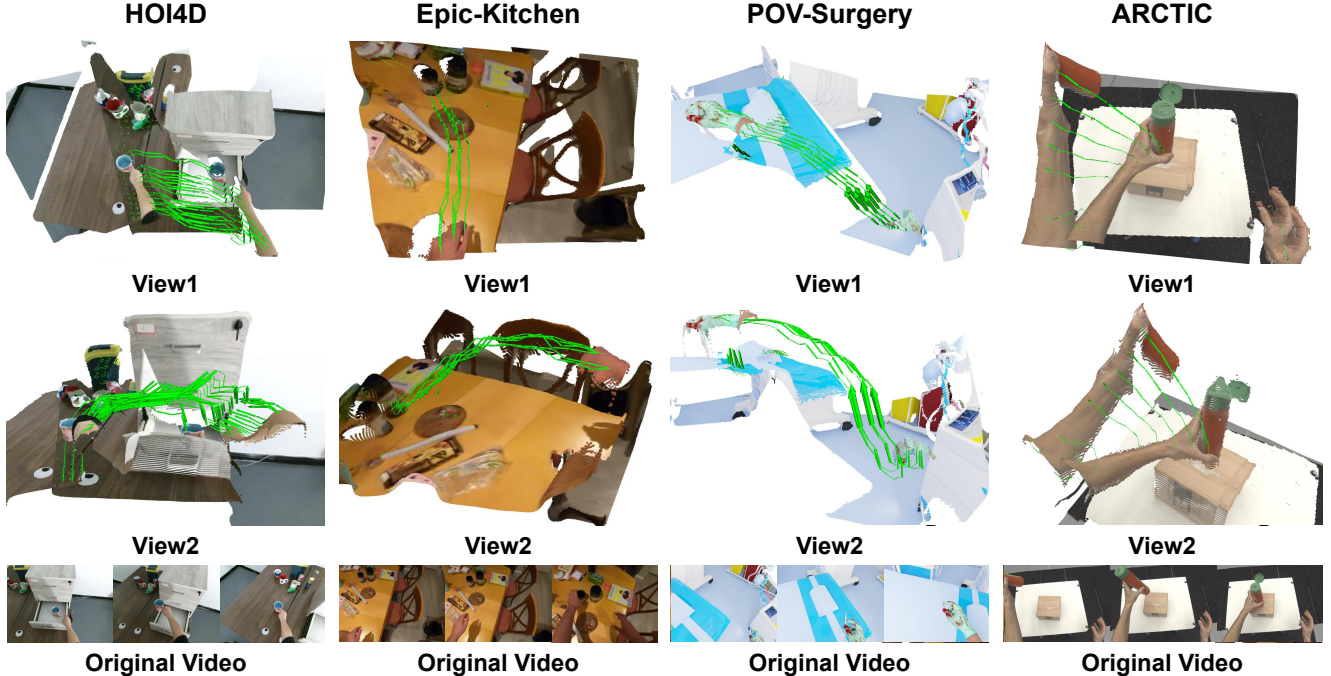


Figure 5. The visualization of the long-term 3D scene flow recovery. For clarity, we display only the pointclouds from the first and last frame. The green arrows representing the estimated 3D flow. UniHOI successfully recovers the motion of dynamic parts while maintaining other regions static to some extent. See Appendix H for more visualization.

Tracker [24], a high-precision pixel tracker, to generate 2D long-term tracking (with a 35×35 grid of query points). These 2D trajectories are then unprojected using ground-truth pointclouds sequence to create 3D trajectory labels. We use the same method to obtain predictions for models.

Metric To align the scale of scenes, we first perform a best-aligned scaled SE(3) transformation between the ground-truth and predicted pointclouds for the first frame. We adopt metrics from related works [3, 30, 75, 87], including Average Displacement Error (ADE, mm), Final Displacement Error (FDE, mm), and Precision under Distance (P, %). We use the notation P_δ to represent precision with a δ centimeter (cm) threshold.

Result Table 3 shows that our model outperforms all baselines on average. DS+UniDepth performs well in hand-object motion estimation on the ARCTIC dataset. We also compared the HOI estimation of both models on three other datasets, with results in Table 4. Both models perform similarly, with UniHOI shows a modest advantage. However, DS+UniDepth’s performance drops notably in full-scene estimation (e.g., POV-Surgery dataset) due to inconsistencies and accumulated errors between modules. Other models perform worse overall. Figure 5 illustrates the estimated long-term 3D scene flow. It can be seen that UniHOI successfully reconstructs 3D dynamics across diverse scenes.

6.3. Inference Speed

We evaluate the inference speed of all models (for 40 frames video). All measurements are conducted on a single NVIDIA GeForce 3090 GPU with a batch size of 1. Results are shown in Figure 4. Our model achieves the fastest speed, except for its modularized version (MFVR+UniDepth).

7. Discussion

We evaluate our model’s sensitivity to video FPS in Appendix E and conduct ablation study in Appendix F. Depth and camera estimation results are presented in Appendix G, demonstrating that UniHOI’s improvements over modularized methods stem from enhanced consistency between geometric variables, rather than individual accuracy.

More visualizations of UniHOI results are available in Appendix H. Qualitative comparison with baselines could be found in Appendix I. It can be seen that DS+UniDepth [49, 70] struggles with static scene alignment, while MonSt3R [90] fails for reconstructing hand geometry.

Below, we briefly highlight the main limitations and possible solutions for UniHOI. For more discussion, please refer to Appendix J. There are two typical failure cases of UniHOI, particularly in videos with significant camera motion. (1) Dynamic part distortion: The size of dynamic objects may vary noticeably; (2) Static part misalignment: static part boundaries can become misaligned over time. These

two issues stem from label-free training and inherent inconsistencies in UniDepth [49] supervision. Incorporating ground-truth depth during training may help alleviate these problems. We offer practical guidance for UniHOI usage in Appendix K.

8. Conclusion

We introduce UniHOI, a unified model for camera intrinsic, poses, and video depth estimation aimed at dense 4D reconstruction of egocentric HOI scene. By leveraging priors from pretrained vision models, UniHOI can be trained on large-scale, unlabeled HOI video datasets. The model delivers promising zero-shot results in dense pointclouds sequence reconstruction and long-term 3D scene flow recovery, marking a first attempt toward fast, dense, and generalizable 4D reconstruction for egocentric HOI videos.

References

- [1] Eduardo Arnold, Jamie Wynn, Sara Vicente, Guillermo Garcia-Hernando, Aron Monszpart, Victor Prisacariu, Daniyar Turmukhambetov, and Eric Brachmann. Map-free visual relocalization: Metric pose relative to a single image. In *European Conference on Computer Vision*, pages 690–708. Springer, 2022. 2, 6
- [2] Shikhar Bahl, Russell Mendonca, Lili Chen, Unnat Jain, and Deepak Pathak. Affordances from human videos as a versatile representation for robotics. In *Proceedings of the IEEE/CVF Conference on Computer Vision and Pattern Recognition*, pages 13778–13790, 2023. 3
- [3] Wentao Bao, Lele Chen, Libing Zeng, Zhong Li, Yi Xu, Junsong Yuan, and Yu Kong. Uncertainty-aware state space transformer for egocentric 3d hand trajectory forecasting. In *Proceedings of the IEEE/CVF International Conference on Computer Vision*, pages 13702–13711, 2023. 2, 3, 7, 8, 14
- [4] Shariq Farooq Bhat, Reiner Birkel, Diana Wofk, Peter Wonka, and Matthias Müller. Zoedepth: Zero-shot transfer by combining relative and metric depth. *arXiv preprint arXiv:2302.12288*, 2023. 2
- [5] Jiawang Bian, Zhichao Li, Naiyan Wang, Huangying Zhan, Chunhua Shen, Ming-Ming Cheng, and Ian Reid. Unsupervised scale-consistent depth and ego-motion learning from monocular video. *Advances in neural information processing systems*, 32, 2019. 2
- [6] Reiner Birkel, Diana Wofk, and Matthias Müller. Midas v3. 1—a model zoo for robust monocular relative depth estimation. *arXiv preprint arXiv:2307.14460*, 2023. 2, 4, 19
- [7] Carlos Campos, Richard Elvira, Juan J Gómez Rodríguez, José MM Montiel, and Juan D Tardós. Orb-slam3: An accurate open-source library for visual, visual-inertial, and multi-map slam. *IEEE Transactions on Robotics*, 37(6):1874–1890, 2021. 2
- [8] Weirong Chen, Le Chen, Rui Wang, and Marc Pollefeys. Leap-vo: Long-term effective any point tracking for visual odometry. In *Proceedings of the IEEE/CVF Conference on Computer Vision and Pattern Recognition*, pages 19844–19853, 2024. 2
- [9] Zhe Chen, Yuchen Duan, Wenhai Wang, Junjun He, Tong Lu, Jifeng Dai, and Yu Qiao. Vision transformer adapter for dense predictions. *arXiv preprint arXiv:2205.08534*, 2022. 4, 13
- [10] Suhwan Cho, Minhyeok Lee, Seunghoon Lee, Chaewon Park, Donghyeong Kim, and Sangyoun Lee. Treating motion as option to reduce motion dependency in unsupervised video object segmentation. In *Proceedings of the IEEE/CVF winter conference on applications of computer vision*, pages 5140–5149, 2023. 20
- [11] Christopher Choy, Wei Dong, and Vladlen Koltun. Deep global registration. In *Proceedings of the IEEE/CVF conference on computer vision and pattern recognition*, pages 2514–2523, 2020. 4
- [12] Wen-Hsuan Chu, Lei Ke, and Katerina Fragkiadaki. Dream-scene4d: Dynamic multi-object scene generation from monocular videos. *arXiv preprint arXiv:2405.02280*, 2024. 3
- [13] Özgün Çiçek, Ahmed Abdulkadir, Soeren S Lienkamp, Thomas Brox, and Olaf Ronneberger. 3d u-net: learning dense volumetric segmentation from sparse annotation. In *Medical Image Computing and Computer-Assisted Intervention—MICCAI 2016: 19th International Conference, Athens, Greece, October 17-21, 2016, Proceedings, Part II 19*, pages 424–432. Springer, 2016. 4, 13
- [14] Zhaopeng Cui and Ping Tan. Global structure-from-motion by similarity averaging. In *Proceedings of the IEEE International Conference on Computer Vision*, pages 864–872, 2015. 2
- [15] Dima Damen, Hazel Doughty, Giovanni Maria Farinella, Antonino Furnari, Evangelos Kazakos, Jian Ma, Davide Moltisanti, Jonathan Munro, Toby Perrett, Will Price, et al. Rescaling egocentric vision: Collection, pipeline and challenges for epic-kitchens-100. *International Journal of Computer Vision*, pages 1–23, 2022. 1, 2, 3, 4, 5, 13
- [16] Alexey Dosovitskiy. An image is worth 16x16 words: Transformers for image recognition at scale. *arXiv preprint arXiv:2010.11929*, 2020. 13
- [17] Ben Eisner, Harry Zhang, and David Held. Flowbot3d: Learning 3d articulation flow to manipulate articulated objects. *arXiv preprint arXiv:2205.04382*, 2022. 7
- [18] Zicong Fan, Omid Taheri, Dimitrios Tzionas, Muhammed Kocabas, Manuel Kaufmann, Michael J Black, and Otmar Hilliges. Arctic: A dataset for dexterous bimanual hand-object manipulation. In *Proceedings of the IEEE/CVF Conference on Computer Vision and Pattern Recognition*, pages 12943–12954, 2023. 3, 4, 5, 13
- [19] Clement Fuji Tsang, Maria Shugrina, Jean Francois Lafleche, Towaki Takikawa, Jiehan Wang, Charles Loop, Wenzheng Chen, Krishna Murthy Jatavallabhula, Edward Smith, Artem Rozantsev, Or Perel, Tianchang Shen, Jun Gao, Sanja Fidler, Gavriel State, Jason Gorski, Tommy Xi-ang, Jianing Li, Michael Li, and Rev Lebedev. Kaolin: A pytorch library for accelerating 3d deep learning research. <https://github.com/NVIDIAGameWorks/kaolin>, 2022. 14

- [20] Guillermo Garcia-Hernando, Shanxin Yuan, Seungryul Baek, and Tae-Kyun Kim. First-person hand action benchmark with rgb-d videos and 3d hand pose annotations. In *Proceedings of the IEEE conference on computer vision and pattern recognition*, pages 409–419, 2018. 2, 3, 4, 5, 13
- [21] Kristen Grauman, Andrew Westbury, Eugene Byrne, Zachary Chavis, Antonino Furnari, Rohit Girdhar, Jackson Hamburger, Hao Jiang, Miao Liu, Xingyu Liu, et al. Ego4d: Around the world in 3,000 hours of egocentric video. In *Proceedings of the IEEE/CVF Conference on Computer Vision and Pattern Recognition*, pages 18995–19012, 2022. 1, 2, 3, 4
- [22] Boris Hanin and David Rolnick. Deep relu networks have surprisingly few activation patterns. *Advances in neural information processing systems*, 32, 2019. 13
- [23] Wenbo Hu, Xiangjun Gao, Xiaoyu Li, Sijie Zhao, Xiaodong Cun, Yong Zhang, Long Quan, and Ying Shan. Depthcrafter: Generating consistent long depth sequences for open-world videos. *arXiv preprint arXiv:2409.02095*, 2024. 2
- [24] Nikita Karaev, Ignacio Rocco, Benjamin Graham, Natalia Neverova, Andrea Vedaldi, and Christian Rupprecht. Co-tracker: It is better to track together. *arXiv preprint arXiv:2307.07635*, 2023. 2, 3, 4, 5, 8, 14
- [25] Yoni Kasten, Wuyue Lu, and Haggai Maron. Fast encoder-based 3d from casual videos via point track processing. In *ECCV 2024 Workshop on Wild 3D: 3D Modeling, Reconstruction, and Generation in the Wild*. 3
- [26] Bernhard Kerbl, Georgios Kopanas, Thomas Leimkühler, and George Drettakis. 3d gaussian splatting for real-time radiance field rendering. *ACM Trans. Graph.*, 42(4):139–1, 2023. 2, 3
- [27] Diederik P Kingma. Adam: A method for stochastic optimization. *arXiv preprint arXiv:1412.6980*, 2014. 6
- [28] Alexander Kirillov, Eric Mintun, Nikhila Ravi, Hanzi Mao, Chloe Rolland, Laura Gustafson, Tete Xiao, Spencer Whitehead, Alexander C Berg, Wan-Yen Lo, et al. Segment anything. In *Proceedings of the IEEE/CVF International Conference on Computer Vision*, pages 4015–4026, 2023. 20
- [29] Johannes Kopf, Xuejian Rong, and Jia-Bin Huang. Robust consistent video depth estimation. In *Proceedings of the IEEE/CVF Conference on Computer Vision and Pattern Recognition*, pages 1611–1621, 2021. 2, 3
- [30] Skanda Koppula, Ignacio Rocco, Yi Yang, Joe Heyward, João Carreira, Andrew Zisserman, Gabriel Brostow, and Carl Doersch. Tapvid-3d: A benchmark for tracking any point in 3d. *arXiv preprint arXiv:2407.05921*, 2024. 2, 3, 7, 8, 14
- [31] Taein Kwon, Bugra Tekin, Jan Stühmer, Federica Bogo, and Marc Pollefeys. H2o: Two hands manipulating objects for first person interaction recognition. In *Proceedings of the IEEE/CVF International Conference on Computer Vision*, pages 10138–10148, 2021. 2, 3, 4, 5, 13
- [32] Jiahui Lei, Yijia Weng, Adam Harley, Leonidas Guibas, and Kostas Daniilidis. Mosca: Dynamic gaussian fusion from casual videos via 4d motion scaffolds. *arXiv preprint arXiv:2405.17421*, 2024. 2, 3
- [33] Vincent Leroy, Yohann Cabon, and Jérôme Revaud. Grounding image matching in 3d with mast3r. *arXiv preprint arXiv:2406.09756*, 2024. 3, 20
- [34] Yiming Li, Ziang Cao, Andrew Liang, Benjamin Liang, Luoyao Chen, Hang Zhao, and Chen Feng. Egocentric prediction of action target in 3d. In *2022 IEEE/CVF Conference on Computer Vision and Pattern Recognition (CVPR)*, pages 20971–20980. IEEE, 2022. 2, 3, 4, 5, 13
- [35] Haokun Liu, Derek Tam, Mohammed Muqeeth, Jay Mohta, Tenghao Huang, Mohit Bansal, and Colin A Raffel. Few-shot parameter-efficient fine-tuning is better and cheaper than in-context learning. *Advances in Neural Information Processing Systems*, 35:1950–1965, 2022. 4
- [36] Shilong Liu, Zhaoyang Zeng, Tianhe Ren, Feng Li, Hao Zhang, Jie Yang, Chunyuan Li, Jianwei Yang, Hang Su, Jun Zhu, et al. Grounding dino: Marrying dino with grounded pre-training for open-set object detection. *arXiv preprint arXiv:2303.05499*, 2023. 20
- [37] Xiaochen Liu, Tao Zhang, and Mingming Liu. Joint estimation of pose, depth, and optical flow with a competition-cooperation transformer network. *Neural Networks*, 171: 263–275, 2024. 2
- [38] Yunze Liu, Yun Liu, Che Jiang, Kangbo Lyu, Weikang Wan, Hao Shen, Boqiang Liang, Zhoujie Fu, He Wang, and Li Yi. Hoi4d: A 4d egocentric dataset for category-level human-object interaction. In *Proceedings of the IEEE/CVF Conference on Computer Vision and Pattern Recognition*, pages 21013–21022, 2022. 2, 3, 4, 5, 13, 15
- [39] Yu-Lun Liu, Chen Gao, Andreas Meuleman, Hung-Yu Tseng, Ayush Saraf, Changil Kim, Yung-Yu Chuang, Johannes Kopf, and Jia-Bin Huang. Robust dynamic radiance fields. In *Proceedings of the IEEE/CVF Conference on Computer Vision and Pattern Recognition*, pages 13–23, 2023. 5
- [40] Jonathon Luiten, Georgios Kopanas, Bastian Leibe, and Deva Ramanan. Dynamic 3d gaussians: Tracking by persistent dynamic view synthesis. *arXiv preprint arXiv:2308.09713*, 2023. 2, 3
- [41] Moritz Menze and Andreas Geiger. Object scene flow for autonomous vehicles. In *Proceedings of the IEEE conference on computer vision and pattern recognition*, pages 3061–3070, 2015. 7
- [42] Yao Mu, Qinglong Zhang, Mengkang Hu, Wenhai Wang, Mingyu Ding, Jun Jin, Bin Wang, Jifeng Dai, Yu Qiao, and Ping Luo. Embodiedgpt: Vision-language pre-training via embodied chain of thought. *Advances in Neural Information Processing Systems*, 36, 2024. 3
- [43] Raul Mur-Artal, Jose Maria Martinez Montiel, and Juan D Tardos. Orb-slam: a versatile and accurate monocular slam system. *IEEE transactions on robotics*, 31(5):1147–1163, 2015. 2, 20
- [44] Suraj Nair, Aravind Rajeswaran, Vikash Kumar, Chelsea Finn, and Abhinav Gupta. R3m: A universal visual representation for robot manipulation. *arXiv preprint arXiv:2203.12601*, 2022. 1, 3
- [45] Maxime Oquab, Timothée Darcet, Théo Moutakanni, Huy Vo, Marc Szafraniec, Vasil Khalidov, Pierre Fernandez, Daniel Haziza, Francisco Massa, Alaaeldin El-Nouby, et al. Dinov2: Learning robust visual features without supervision. *arXiv preprint arXiv:2304.07193*, 2023. 13
- [46] Evin Pinar Örnek, Shristi Mudgal, Johanna Wald, Yida Wang, Nassir Navab, and Federico Tombari. From 2d to

- 3d: Re-thinking benchmarking of monocular depth prediction. *arXiv preprint arXiv:2203.08122*, 2022. 7, 14
- [47] Xiaqing Pan, Nicholas Charron, Yongqian Yang, Scott Peters, Thomas Whelan, Chen Kong, Omkar Parkhi, Richard Newcombe, and Yuheng Carl Ren. Aria digital twin: A new benchmark dataset for egocentric 3d machine perception. In *Proceedings of the IEEE/CVF International Conference on Computer Vision*, pages 20133–20143, 2023. 1, 3, 20
- [48] Georgios Pavlakos, Dandan Shan, Ilija Radosavovic, Angjoo Kanazawa, David Fouhey, and Jitendra Malik. Reconstructing hands in 3d with transformers. In *Proceedings of the IEEE/CVF Conference on Computer Vision and Pattern Recognition*, pages 9826–9836, 2024. 3
- [49] Luigi Piccinelli, Yung-Hsu Yang, Christos Sakaridis, Mattia Segu, Siyuan Li, Luc Van Gool, and Fisher Yu. Unidepth: Universal monocular metric depth estimation. In *Proceedings of the IEEE/CVF Conference on Computer Vision and Pattern Recognition*, pages 10106–10116, 2024. 2, 3, 4, 5, 6, 7, 8, 9, 13, 18, 19, 20
- [50] Rolandos Alexandros Potamias, Jinglei Zhang, Jiankang Deng, and Stefanos Zafeiriou. Wilor: End-to-end 3d hand localization and reconstruction in-the-wild. *arXiv preprint arXiv:2409.12259*, 2024. 3
- [51] Shraman Pramanick, Yale Song, Sayan Nag, Kevin Qinghong Lin, Hardik Shah, Mike Zheng Shou, Rama Chellappa, and Pengchuan Zhang. Egovlpv2: Egocentric video-language pre-training with fusion in the backbone. In *Proceedings of the IEEE/CVF International Conference on Computer Vision*, pages 5285–5297, 2023. 1
- [52] Shengyi Qian, Weifeng Chen, Min Bai, Xiong Zhou, Zhuowen Tu, and Li Erran Li. Affordancellm: Grounding affordance from vision language models. In *Proceedings of the IEEE/CVF Conference on Computer Vision and Pattern Recognition*, pages 7587–7597, 2024. 3
- [53] Yuzhe Qin, Hao Su, and Xiaolong Wang. From one hand to multiple hands: Imitation learning for dexterous manipulation from single-camera teleoperation. *IEEE Robotics and Automation Letters*, 7(4):10873–10881, 2022. 3
- [54] Uchitha Rajapaksha, Ferdous Sohel, Hamid Laga, Dean Diepeveen, and Mohammed Bennamoun. Deep learning-based depth estimation methods from monocular image and videos: A comprehensive survey. *ACM Computing Surveys*, 2024. 2
- [55] Antoni Rosinol, John J Leonard, and Luca Carlone. Nerfslam: Real-time dense monocular slam with neural radiance fields. In *2023 IEEE/RSJ International Conference on Intelligent Robots and Systems (IROS)*, pages 3437–3444. IEEE, 2023. 2
- [56] Alexander Sabov and Jörg Krüger. Identification and correction of flying pixels in range camera data. In *Proceedings of the 24th Spring Conference on Computer Graphics*, pages 135–142, 2008. 5, 14
- [57] Johannes L Schonberger and Jan-Michael Frahm. Structure-from-motion revisited. In *Proceedings of the IEEE conference on computer vision and pattern recognition*, pages 4104–4113, 2016. 2
- [58] Johannes L Schönberger, Enliang Zheng, Jan-Michael Frahm, and Marc Pollefeys. Pixelwise view selection for unstructured multi-view stereo. In *Computer Vision—ECCV 2016: 14th European Conference, Amsterdam, The Netherlands, October 11–14, 2016, Proceedings, Part III 14*, pages 501–518. Springer, 2016. 2
- [59] Daniel Seita, Yufei Wang, Sarthak J Shetty, Edward Yao Li, Zackory Erickson, and David Held. Toolflownet: Robotic manipulation with tools via predicting tool flow from point clouds. In *Conference on Robot Learning*, pages 1038–1049. PMLR, 2023. 7
- [60] Dandan Shan, Jiaqi Geng, Michelle Shu, and David F Fouhey. Understanding human hands in contact at internet scale. In *Proceedings of the IEEE/CVF conference on computer vision and pattern recognition*, pages 9869–9878, 2020. 3
- [61] Lin Shao, Parth Shah, Vikranth Dwaracherla, and Jeannette Bohg. Motion-based object segmentation based on dense rgb-d scene flow. *IEEE Robotics and Automation Letters*, 3(4):3797–3804, 2018. 7
- [62] Dongseok Shim and H Jin Kim. Swindepth: Unsupervised depth estimation using monocular sequences via swin transformer and densely cascaded network. In *2023 IEEE International Conference on Robotics and Automation (ICRA)*, pages 4983–4990. IEEE, 2023. 2
- [63] Cameron Smith, Yilun Du, Ayush Tewari, and Vincent Sitzmann. Flowcam: training generalizable 3d radiance fields without camera poses via pixel-aligned scene flow. *arXiv preprint arXiv:2306.00180*, 2023. 2, 4
- [64] Cameron Smith, David Charatan, Ayush Tewari, and Vincent Sitzmann. Flowmap: High-quality camera poses, intrinsics, and depth via gradient descent. *arXiv preprint arXiv:2404.15259*, 2024. 2, 4, 5, 7, 13, 19
- [65] Jaime Spencer, Chris Russell, Simon Hadfield, and Richard Bowden. Kick back & relax: Learning to reconstruct the world by watching slowtv. In *Proceedings of the IEEE/CVF International Conference on Computer Vision*, pages 15768–15779, 2023. 2, 5
- [66] Jaime Spencer, Chris Russell, Simon Hadfield, and Richard Bowden. Kick back & relax++: Scaling beyond ground-truth depth with slowtv & cribstv. *arXiv preprint arXiv:2403.01569*, 2024. 2
- [67] Yukun Su, Jingliang Deng, Ruizhou Sun, Guosheng Lin, Hanjing Su, and Qingyao Wu. A unified transformer framework for group-based segmentation: Co-segmentation, saliency detection and video salient object detection. *IEEE Transactions on Multimedia*, 26:313–325, 2023. 20
- [68] Jiakai Sun, Han Jiao, Guangyuan Li, Zhanjie Zhang, Lei Zhao, and Wei Xing. 3dstream: On-the-fly training of 3d gaussians for efficient streaming of photo-realistic free-viewpoint videos. In *Proceedings of the IEEE/CVF Conference on Computer Vision and Pattern Recognition*, pages 20675–20685, 2024. 2, 3
- [69] Yihong Sun and Bharath Hariharan. Dynamo-depth: fixing unsupervised depth estimation for dynamical scenes. *Advances in Neural Information Processing Systems*, 36, 2024. 2
- [70] Zachary Teed and Jia Deng. Droid-slam: Deep visual slam for monocular, stereo, and rgb-d cameras. *Advances in neu-*

- ral information processing systems*, 34:16558–16569, 2021. [2](#), [6](#), [8](#), [18](#), [20](#)
- [71] Vicon Vantage. Cutting edge, flagship camera with intelligent feedback and resolution. [5](#)
- [72] A Vaswani. Attention is all you need. *Advances in Neural Information Processing Systems*, 2017. [4](#), [13](#)
- [73] Sundar Vedula, Simon Baker, Peter Rander, Robert Collins, and Takeo Kanade. Three-dimensional scene flow. In *Proceedings of the Seventh IEEE International Conference on Computer Vision*, pages 722–729. IEEE, 1999. [7](#)
- [74] Jianyuan Wang, Nikita Karaev, Christian Rupprecht, and David Novotny. Vggsfm: Visual geometry grounded deep structure from motion. In *Proceedings of the IEEE/CVF Conference on Computer Vision and Pattern Recognition*, pages 21686–21697, 2024. [2](#), [20](#)
- [75] Qianqian Wang, Vickie Ye, Hang Gao, Jake Austin, Zhengqi Li, and Angjoo Kanazawa. Shape of motion: 4d reconstruction from a single video. *arXiv preprint arXiv:2407.13764*, 2024. [2](#), [3](#), [8](#)
- [76] Rui Wang, Sophokles Ktistakis, Siwei Zhang, Mirko Meboldt, and Quentin Lohmeyer. Pov-surgery: A dataset for egocentric hand and tool pose estimation during surgical activities. In *International Conference on Medical Image Computing and Computer-Assisted Intervention*, pages 440–450. Springer, 2023. [2](#), [3](#), [4](#), [5](#), [13](#), [15](#), [16](#), [19](#)
- [77] Shuzhe Wang, Vincent Leroy, Yohann Cabon, Boris Chidlovskii, and Jerome Revaud. Dust3r: Geometric 3d vision made easy. In *Proceedings of the IEEE/CVF Conference on Computer Vision and Pattern Recognition*, pages 20697–20709, 2024. [1](#), [2](#), [3](#), [6](#), [7](#), [20](#)
- [78] Wenshan Wang, Yaoyu Hu, and Sebastian Scherer. Tartanvo: A generalizable learning-based vo. In *Conference on Robot Learning*, pages 1761–1772. PMLR, 2021. [2](#)
- [79] Yiran Wang, Min Shi, Jiaqi Li, Zihao Huang, Zhiguo Cao, Jianming Zhang, Ke Xian, and Guosheng Lin. Neural video depth stabilizer. In *Proceedings of the IEEE/CVF International Conference on Computer Vision*, pages 9466–9476, 2023. [2](#)
- [80] Ying Wang, Dongdong Sun, Rui Chen, Yanlai Yang, and Mengye Ren. Egocentric video comprehension via large language model inner speech. In *3rd International Ego4D Workshop*, 2023. [3](#)
- [81] Chuan Wen, Xingyu Lin, John So, Kai Chen, Qi Dou, Yang Gao, and Pieter Abbeel. Any-point trajectory modeling for policy learning. *arXiv preprint arXiv:2401.00025*, 2023. [3](#)
- [82] Junyu Xie, Charig Yang, Weidi Xie, and Andrew Zisserman. Moving object segmentation: All you need is sam (and flow). *arXiv preprint arXiv:2404.12389*, 2024. [20](#)
- [83] Haofei Xu, Jing Zhang, Jianfei Cai, Hamid Rezatofighi, and Dacheng Tao. Gmflow: Learning optical flow via global matching. In *Proceedings of the IEEE/CVF conference on computer vision and pattern recognition*, pages 8121–8130, 2022. [2](#), [3](#), [4](#), [5](#), [6](#), [13](#), [16](#), [20](#)
- [84] Lihe Yang, Bingyi Kang, Zilong Huang, Xiaogang Xu, Jiashi Feng, and Hengshuang Zhao. Depth anything: Unleashing the power of large-scale unlabeled data. In *Proceedings of the IEEE/CVF Conference on Computer Vision and Pattern Recognition*, pages 10371–10381, 2024. [2](#)
- [85] Zhenheng Yang, Peng Wang, Yang Wang, Wei Xu, and Ram Nevatia. Every pixel counts: Unsupervised geometry learning with holistic 3d motion understanding. In *Proceedings of the European conference on computer vision (ECCV) workshops*, pages 0–0, 2018. [2](#)
- [86] Wei Yin, Chi Zhang, Hao Chen, Zhipeng Cai, Gang Yu, Kaixuan Wang, Xiaozhi Chen, and Chunhua Shen. Metric3d: Towards zero-shot metric 3d prediction from a single image. In *Proceedings of the IEEE/CVF International Conference on Computer Vision*, pages 9043–9053, 2023. [2](#)
- [87] Chengbo Yuan, Chuan Wen, Tong Zhang, and Yang Gao. General flow as foundation affordance for scalable robot learning. *arXiv preprint arXiv:2401.11439*, 2024. [1](#), [2](#), [3](#), [7](#), [8](#), [14](#)
- [88] Raza Yunus, Jan Eric Lenssen, Michael Niemeyer, Yiyi Liao, Christian Rupprecht, Christian Theobalt, Gerard Pons-Moll, Jia-Bin Huang, Vladislav Golyanik, and Eddy Ilg. Recent trends in 3d reconstruction of general non-rigid scenes. In *Computer Graphics Forum*, page e15062. Wiley Online Library, 2024. [2](#), [3](#)
- [89] Daiwei Zhang, Gengyan Li, Jiajie Li, Mickaël Bressieux, Otmar Hilliges, Marc Pollefeys, Luc Van Gool, and Xi Wang. Egogaussian: Dynamic scene understanding from egocentric video with 3d gaussian splatting. *arXiv preprint arXiv:2406.19811*, 2024. [2](#), [3](#)
- [90] Junyi Zhang, Charles Herrmann, Junhwa Hur, Varun Jampani, Trevor Darrell, Forrester Cole, Deqing Sun, and Ming-Hsuan Yang. Monst3r: A simple approach for estimating geometry in the presence of motion. *arXiv preprint arXiv:2410.03825*, 2024. [1](#), [3](#), [6](#), [7](#), [8](#), [18](#), [19](#), [20](#)
- [91] Lingzhi Zhang, Shenghao Zhou, Simon Stent, and Jianbo Shi. Fine-grained egocentric hand-object segmentation: Dataset, model, and applications. In *European Conference on Computer Vision*, pages 127–145. Springer, 2022. [1](#), [2](#), [3](#), [4](#), [5](#), [6](#)
- [92] Youmin Zhang, Fabio Tosi, Stefano Mattoccia, and Matteo Poggi. Go-slam: Global optimization for consistent 3d instant reconstruction. In *Proceedings of the IEEE/CVF International Conference on Computer Vision*, pages 3727–3737, 2023. [2](#)
- [93] Zhoutong Zhang, Forrester Cole, Zhengqi Li, Michael Rubinstein, Noah Snavely, and William T Freeman. Structure and motion from casual videos. In *European Conference on Computer Vision*, pages 20–37. Springer, 2022. [3](#)
- [94] Wang Zhao, Shaohui Liu, Hengkai Guo, Wenping Wang, and Yong-Jin Liu. Particlesfm: Exploiting dense point trajectories for localizing moving cameras in the wild. In *European Conference on Computer Vision*, pages 523–542. Springer, 2022. [2](#)
- [95] Yang Zheng, Adam W Harley, Bokui Shen, Gordon Wetstein, and Leonidas J Guibas. Pointodyssey: A large-scale synthetic dataset for long-term point tracking. In *Proceedings of the IEEE/CVF International Conference on Computer Vision*, pages 19855–19865, 2023. [3](#), [20](#)

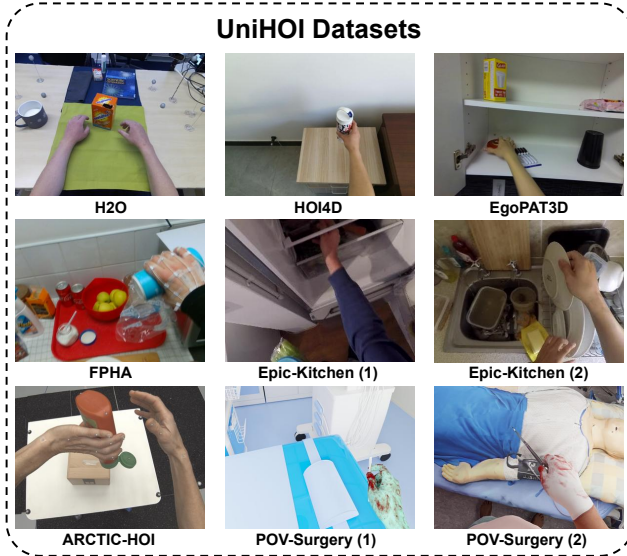


Figure 6. The samples from the datasets used in UniHOI training and evaluation. These data cover different types of egocentric HOI videos, featuring small/large camera motion, simple/complex actions, and clean/cluttered scenes (Table 5).

Appendix

A. Details of Datasets

Figure 6 visualizes samples from various datasets. Detailed information about the datasets is shown in Table 5. The data encompass different types of egocentric HOI videos, with variations in camera motion (small/large), action complexity (simple/complex), and scene conditions (clean/cluttered).

For training, we use a combination of H2O[31] (40K frames), HOI4D[38] (540K frames), FPHA[20] (73K frames), EgoPAT3D[34] (823K frames), and Epic-Kitchen[15] (9.7M frames). The final training dataset contains a total of 11.2M frames, with Epic-Kitchen dominating the data (about 85%), providing large-scale diversity and a wide range of behavior modes. The other datasets contribute unique scene characteristics or behavior patterns. For instance, H2O[31] exclusively contains bi-manual operations with small camera motion in clean table scenes. Approximately 5% of the data is allocated for model validation.

For evaluation, we note a scarcity of egocentric HOI datasets offering both high-quality depth and precise camera labels. We strongly encourage the computer vision and HOI communities to collect or synthesize larger-scale RGBD datasets with accurate pose annotations. We selected four datasets that meet the necessary criteria: H2O[31], HOI4D[38], ARCTIC[18], and POV-Surgery[76]. The sources for camera labels are provided in Table 5.

H2O[31] and HOI4D[38] feature simple scenes and actions and are used as test benchmarks for in-domain prediction performance. For zero-shot generalization evaluation, we use ARCTIC[18] and POV-Surgery[76]. ARCTIC[18] only provides labels for hands and objects, which is why we refer to it as ARCTIC-HOI. It is primarily used to assess the reconstruction quality of HOI. Both ARCTIC-HOI and POV-Surgery present significant challenges for UniHOI, as they exhibit a large domain gap from the training data. (1) For ARCTIC-HOI, the hand and object components occupy a much larger portion of the images compared to the training data. (2) For POV-Surgery, the dataset’s unrealistic textures create a substantial visual domain gap, and the surgical scenes were not encountered during training.

B. Details of Architecture

Our architecture builds upon the UniDepth backbone [49]. UniDepth decouples the tasks of depth and camera estimation by transforming the scene from Cartesian coordinates to a pseudo-spherical representation, which enables dense camera prediction in spherical space. It then incorporates scene scale information from the camera prediction into the depth estimation module using Laplace Spherical Harmonic Encoding (SHE) and a cross-attention mechanism [16, 72].

Our model processes N_w input images, extracting features from each frame individually through the encoder. The UniDepth encoder produces two types of features: (1) DINO [45] features $F_{dino} \in \mathbb{R}^{T \times \frac{H}{s_h} \times \frac{W}{s_w} \times D_{dino}}$, where $s_h \times s_w$ represents the patch size in DINO and D_{dino} is the feature dimension, and (2) global token features $F_{global} \in \mathbb{R}^{T \times D_{global}}$. To fuse the features across time, we incorporate multiple adaptors [9]. Global token features are fused using a Transformer [72], while the patched DINO [45] features are fused using Unet3D [13]. The architecture for the depth and intrinsic decoders remains unchanged from the original UniDepth implementation.

The confidence map decoder is adopted on [64], which is a 3-layer MLP with ReLU [22] activation. The decoder takes a concatenation of (1) fused shallow features from the video adaptors, (2) depth features and confidence maps from the UniDepth decoder [49], and (3) an interpolation of the above features, induced by optical flow [83] from neighboring frames (Section 3.2). A sigmoid function is applied to normalize the final confidence score within the range $[0, 1]$.

C. Details of Evaluation Metrics

We provide the mathematical definitions of the metrics used to evaluate the performance of 3D point cloud sequence reconstruction and long-term 3D scene flow recovery.

Training						
Datasets	# of frames	Data Split	Camera Motion	Action	Scene	Note
H2O	40K	Original Split	Small	Simple	Clean	Bi-manual
HOI4D	540K	Room ID	Medium	Simple	Clean	
FPHA	73K	Task	Medium	Complex	Clutter	Only pick & place
EgoPAT3D	823K	Scene ID	Large	Medium	Medium	
Epic-Kitchen	9.7M	Scene ID	Large	Complex	Clutter	
Evaluation						
Datasets	# of frames	Label	Camera Motion	Action	Scene	Note
H2O	8K	Calibration	Small	Simple	Clean	Bi-manual
HOI4D	12K	SfM	Medium	Simple	Clean	Contain noise
ARCTIC-HOI	13K	Mocap	Medium	Complex	Clean	Only hand and object label
POV-Surgery	26K	Synthesis	Large	Medium	Clutter	Unrealistic texture

Table 5. Comparison of Different Datasets for Training and Evaluation

C.1. Metrics for Pointclouds Sequence

We follow Örnek et al. [46] in using 3D Chamfer Distance (CD, measured in millimeters) and the 3D Pointclouds F-score (F, measured as a percentage %) to evaluate shape similarity. For implementation, we leverage the Kaolin library [19]. Given the ambiguity in the scale of pointclouds, we first align the predicted point cloud sequence to the ground truth using an estimated best-aligned global scaled SE(3) transformation (s, R, T) .

3D Chamfer Distance (CD, mm). Given the predicted per-frame pointclouds $P \in R^{N \times 3}$ and the ground-truth $G \in R^{N \times 3}$, where N is the number of points, the 3D Chamfer Distance (CD) is defined as:

$$CD(R, G) = \sum_{x \in G} \min_{y \in R} \|x - y\| + \sum_{y \in R} \min_{x \in G} \|x - y\| \quad (11)$$

3D Pointclouds F-score (F). The 3D F-score combines precision and recall to provide a balanced evaluation of the predicted surface quality. In the context of 3D pointclouds, precision measures how many points from the predicted surface are close to the ground truth surface, while recall measures how many ground truth points are captured by the predicted surface. Given a distance δ as the positive threshold, the precision $P_\delta(R, G)$, recall $R_\delta(R, G)$ and F-score $F_\delta(R, G)$ are defined as:

$$P_\delta(R, G) = \frac{1}{|R|} \sum_{y \in R} [d_{y \rightarrow G} < \delta] \quad (12)$$

$$R_\delta(R, G) = \frac{1}{|G|} \sum_{x \in G} [d_{x \rightarrow R} < \delta] \quad (13)$$

$$F_\delta(R, G) = \frac{2P_\delta(R, G)R_\delta(R, G)}{P_\delta(R, G) + R_\delta(R, G)} \quad (14)$$

C.2. Metrics for Long-term 3D Scene Flow

Long-term 3D scene flow refers to predicting the future trajectories of multiple 3D query points in the pointclouds of the first frame [87]. Following previous works [3, 30, 87], we evaluate the precision of 3D flow recovery using three metrics: Average Displacement Error (ADE, measured in millimeters), Final Displacement Error (FDE, measured in millimeters), and Precision under Distance (P, measured as a percentage %). The 3D flow is generated by interpolating between the predicted and ground-truth pointclouds based on 2D tracking from CoTracker [24]. Before evaluation, we filter out trajectories affected by noise from flying pixels [56] using ground-truth depth information. To align the scale of scenes and the initial position of the 3D query points, we first perform a best-aligned scaled SE(3) transformation between the ground-truth and predicted pointclouds for the first frame.

Average Displacement Error (ADE, mm). Given the predicted 3D flow $F \in R^{T \times N \times 3}$ and ground-truth flow $G \in R^{T \times N \times 3}$, where T represents the number of frames and N represents the number of trajectories, ADE measures the average displacement across all timestamps.

$$ADE(F, G) = \frac{1}{N} \sum_{i=1}^N \|F_i - G_i\| \quad (15)$$

Final Displacement Error (FDE, mm). FDE measures the displacement of the final timestamp.

$$FDE(F, G) = \|F_{T-1} - G_{T-1}\| \quad (16)$$

Precision under Distance (P, %). The precision metric measures the average percentage of points with an error

N_w	N_o	HOI4D				POV-Surgery			
		CD↓	F ₁ ↑	F _{2.5} ↑	F ₅ ↑	CD↓	F ₁ ↑	F _{2.5} ↑	F ₅ ↑
4	1	5.9	27.9	59.6	83.1	33.8	13.5	32	53.9
2	1	17.9	11.5	29.4	51.6	/	/	/	/
8	1	6.4	26.0	55.6	80.0	35.2	12.6	30.8	53.1
12	1	6.7	25.1	53.5	78.4	/	/	/	/
4	2	5.9	27.9	59.7	83.1	34.6	13.4	32	53.9
4	3	5.9	27.9	59.7	83.1	35.0	13.4	31.9	53.8
8	4	/	/	/	/	36.3	16.6	30.5	52.6

Table 6. Comparison of pointclouds sequence reconstruction results across different window sizes (N_w) and overlapping sizes (N_o). Our model demonstrates robustness to variations in N_o , while maintaining consistency in N_w between training and inference is essential.

	POV-Surgery			
	CD↓	F ₁ ↑	F _{2.5} ↑	F ₅ ↑
fps / 1	25.5	14.2	33.3	54.8
fps / 2	25.4	13.8	32.8	54.9
fps / 4	25.2	14.1	33.1	55.1
fps / 12	28.5	13.0	31.0	53.5

Table 7. The POV-Surgery point cloud sequence reconstruction results across different frames per second (fps) settings.

within δ centimeters (cm).

$$P_\delta = \frac{1}{N} \sum_{i=1}^N [\|F_i - G_i\| < \delta] \quad (17)$$

D. Ablation on Inference Strategy

During inference, our model processes N_w frames in a single feed-forward prediction. Theoretically, the window size N_w can be any value greater than 1. For videos with more frames than N_w , the overlapping size N_o between neighboring windows must also be determined. By default, we set $N_w = 4$ (consistent with training) and $N_o = 1$ (to optimize inference speed). We evaluate the impact of N_w and N_o on reconstruction performance using the pointclouds sequence reconstruction task on HOI4D [38] and POV-Surgery [76], with results shown in Table 6.

For the window size N_w , maintaining consistency between training and inference is crucial, likely because the video adapter is trained specifically to fuse 4 frames. Regarding overlapping size N_o , the model exhibits comparable performance for $N_o = 1, 2, 3$. Therefore, we select $N_o = 1$ to maximize inference speed.

	POV-Surgery (Video Depth)		
	AbsRel↓	$\delta_{0.05}$ ↑	$\delta_{0.1}$ ↑
UniDepth	11.9	<u>40.8</u>	64.7
DUST3R	19.7	31.5	51.9
MonSt3R	18.6	33.6	52.8
UniHOI (Ours)	<u>12.6</u>	41.1	<u>63.9</u>

	POV-Surgery (Camera Poses)		
	ATE↓	RPE-T↓	RPE-R↓
DS+UniDepth	<u>9.05</u>	4.17	<u>0.39</u>
MFVR+UniDepth	47.03	4.10	4.18
MonSt3R	6.63	2.41	0.26
UniHOI (Ours)	11.54	<u>4.01</u>	0.43

Table 8. Result of POV-Surgery video depth and camera poses estimation. It shows that our model does not outperform others in estimating these geometric variables. Instead, our model focus on improving their consistency in 3D space, which leads to better pointclouds sequence reconstruction.

	CD	F ₁	F _{2.5}	F ₅
complete	6.3	26.9	56.9	81.4
w/ midas-loss	6.3 ·	26.1 ↓	56.2 ↓	80.4 ↓
w/ 2d-flow-loss	6.2 ↑	26.7 ↓	57.0 ↑	81.0 ↓
w/o maps-reg	6.5 ↓	23.9 ↓	53.3 ↓	79.0 ↓
w/o cc-loss	6.3 ·	25.2 ↓	56.4 ↓	81.1 ↓

Table 9. Ablation study of the UniHOI model with 2.5% training data on the HOI4D dataset. ↓ indicates performance degradation relative to the complete model, while ↑ indicates improvement. The complete model achieves moderately better performance on average compared to other variants.

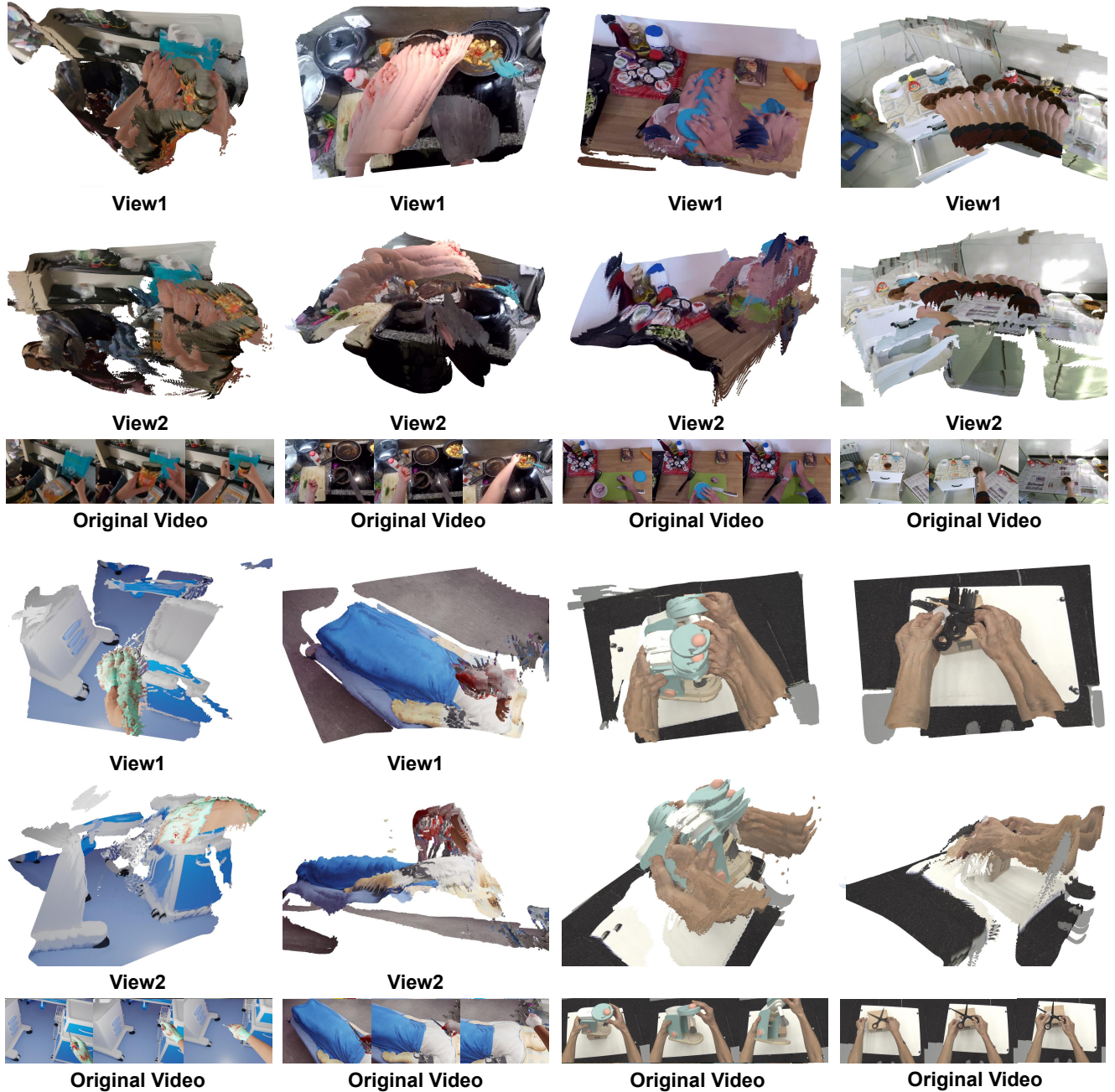


Figure 7. More visualization of pointclouds sequence reconstruction results from UniHOI.

E. Ablation on Video FPS

Since we use random frame intervals to sample data during training, our model is expected to be robust to variations in video fps to some extent. We test this on the pointclouds sequence reconstruction task using the zero-shot dataset POV-Surgery [76]. For a 40-frame sub-clip of POV-Surgery, we select only frames 0, 12, 24, and 36 for evaluation. We define a $1/x$ fps video as a frame sequence sampled with an

interval of x (where 12 should be divisible by x). The evaluation results are shown in Table 7, and they demonstrate that our method is robust to changes in video fps within a certain range. However, when the fps becomes too low, performance degrades, likely because the optical flow module [83] we rely on may fail under such conditions.

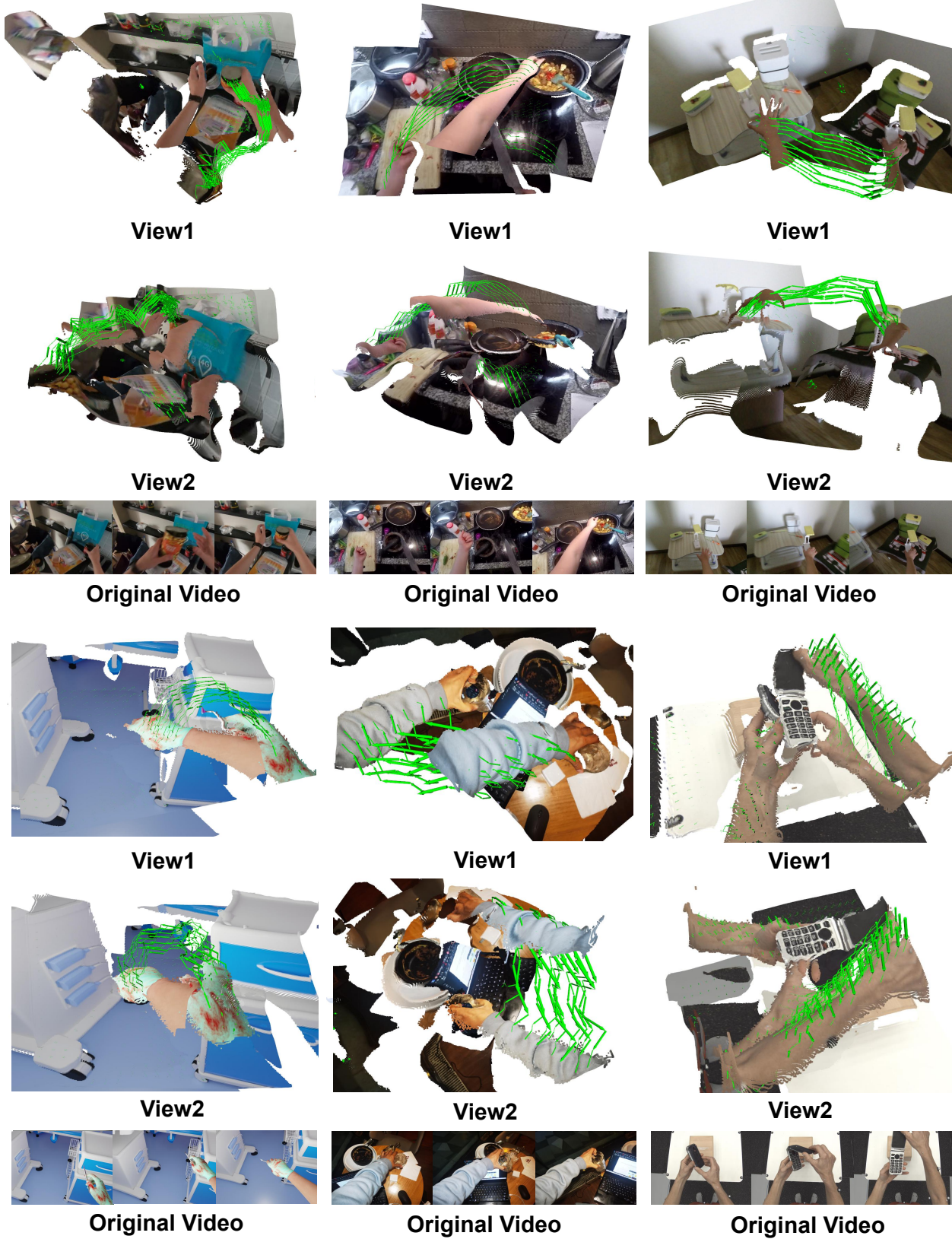


Figure 8. More visualization of long-term 3D scene flow recovery results from UniHOI.

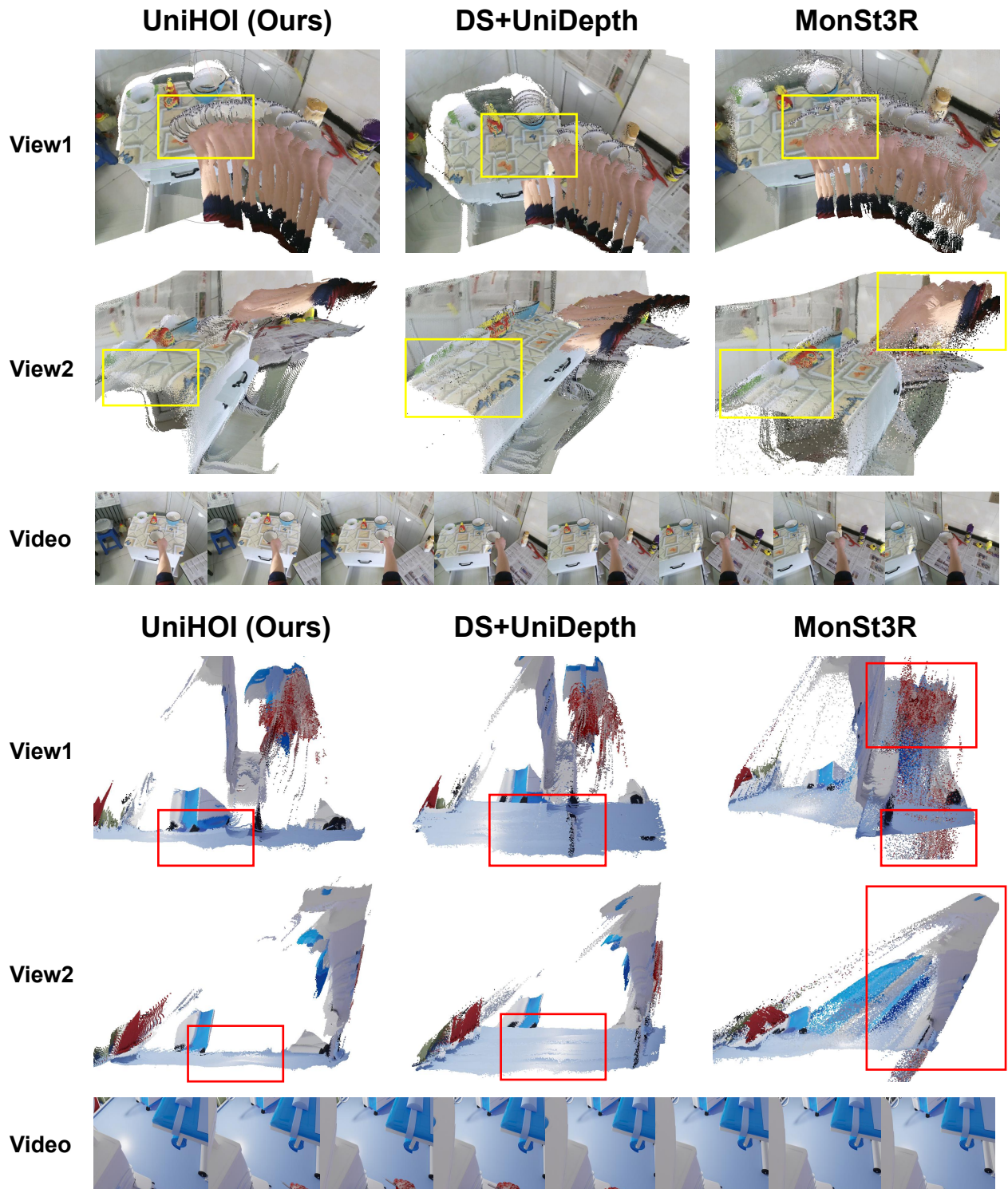


Figure 9. Qualitative comparison between UniHOI and other baseline methods. UniHOI demonstrates superior performance compared to baseline methods in both static scene reconstruction and dynamic HOI motion recovery. DS+UniDepth [49, 70] struggles with static scene alignment, while MonSt3R [90] exhibits limitations in accurately reconstructing hand geometry.

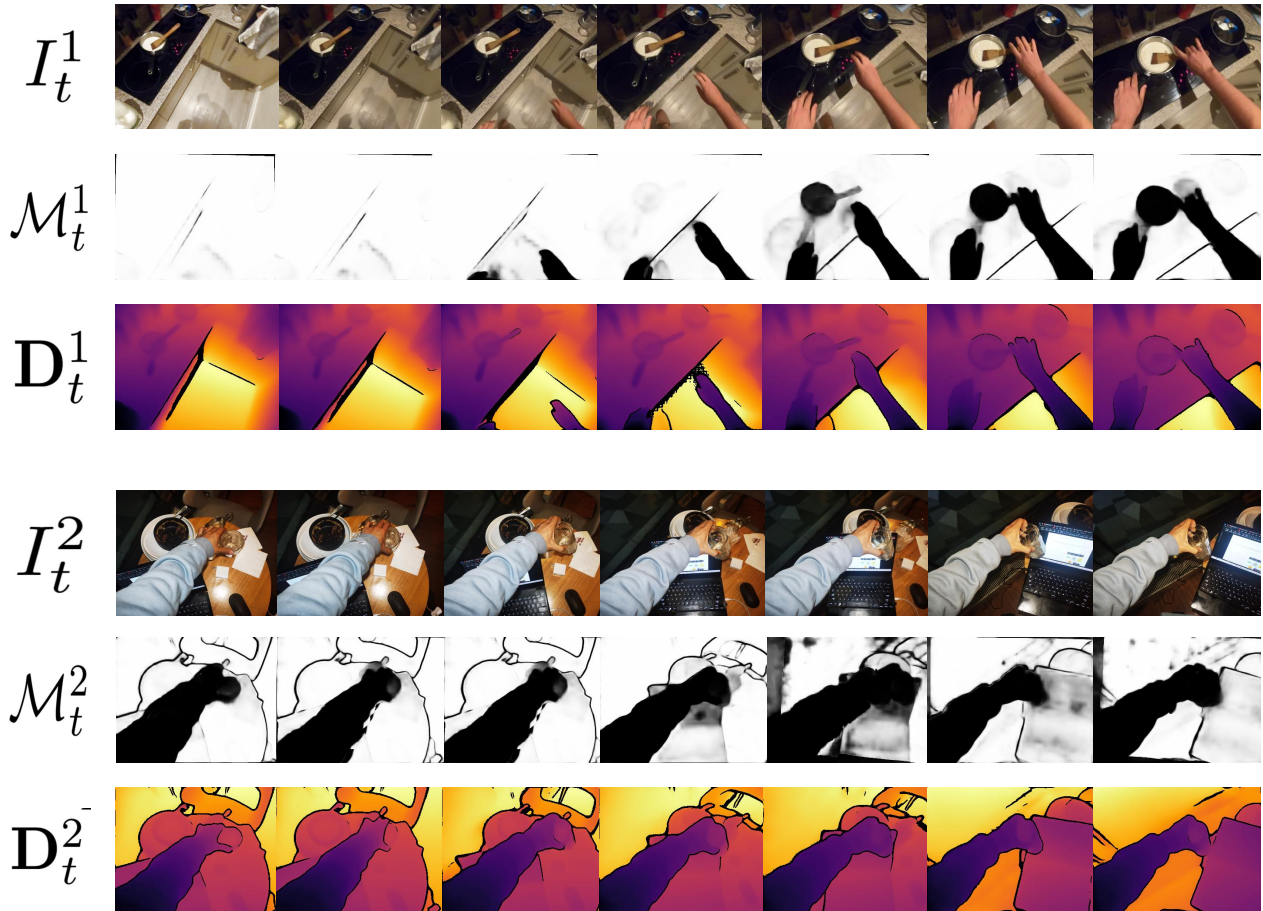


Figure 10. Visualization of original video I_t and the predicted procrustes-alignment confidence maps \mathcal{M}_t and video depth D_t from UniHOI.

F. Ablation on Supervision Signals

We conduct an ablation study of UniHOI using 2.5% training data, evaluating its pointclouds reconstruction performance on the HOI4D dataset. Variants are: (1) w/ midas-loss: replacing \mathcal{L}_{shape} with depth supervision at a relative scale [6]; (2) 2d-flow-loss: substituting $\mathcal{L}_{flow/track}$ with its 2D version in pixel space [64]; (3) w/o maps-reg: removing the confidence maps regularization loss \mathcal{L}_{maps} ; and (4) w/o cc-loss: removing the self-supervised intrinsic loss \mathcal{L}_{cc} .

Results are presented in Table 9. The complete model achieves moderately better performance on average than other variants. Overall, The performance differences among variants are considerably smaller compared to the gap between the base model (even with only 2.5% data) and other baseline methods. This suggests that the unified estimation/optimization paradigm may be the most critical design element of UniHOI, rather than the individual modules.

G. Depth and Camera Results

We further evaluate the video depth and camera poses estimation performance on POV-Surgery [76], using the metrics from MonSt3R [90]. The results are presented in Table 8. Our model does not outperform other methods in estimating these independent geometric variables. Instead, it enhances the consistency of them in 3D space, leading to improved pointclouds sequence reconstruction results. UniDepth [49] achieves the best depth estimation, while MonSt3R [90] provides the most accurate camera poses.

H. More Reconstruction Results Visualization

We provide more visualization of pointclouds sequence reconstruction results of UniHOI in Figure 7. More visualization of recovered long-term 3D scene flows are shown in Figure 8. Finally, we provide the visualization of intermediate geometric variables in Figure 10.



Figure 11. Two typical failure cases of UniHOI arise from inherent inconsistencies in UniDepth shape supervision.

I. Qualitative Comparison with Baseline

We qualitatively compare UniHOI with other baseline methods on the dense point cloud sequence reconstruction task. Visual comparisons are presented in Figure 9. UniHOI demonstrates superior performance compared to baseline methods in both static scene reconstruction and dynamic HOI motion recovery. DS+UniDepth [49, 70] struggles with static scene alignment, while MonSt3R [90] exhibits limitations in accurately reconstructing hand geometry and dynamics.

J. More Limitations and Future Directions

While UniHOI achieves impressive results in fast, dense, and generalizable dynamic HOI scene reconstruction, it still faces challenges with shape misalignment (see Figure 5 in the main paper). This issue arises from inherent inconsistencies in UniDepth’s [49] shape regularization and can be divided into two key problems. (1) Dynamic part (size) distortion: since we only regularize the shape of the dynamic part based on per-frame pointclouds predictions from UniDepth, the relative size of the dynamic part compared to the static part is determined by UniDepth’s predictions. Any inaccuracy in this relative size may be carried over to UniHOI. (2) Static part misalignment: if the original predicted shapes of the static areas from UniDepth differ significantly between frames, it becomes difficult to adjust and align them consistently.

Although precise posed datasets are limited, there are more datasets available with depth labels. Training on these datasets with ground-truth shape supervision, or using a combination of labeled and unlabeled datasets, could help address these issues. Improvements in monocular depth estimation and intrinsic parameter estimation may also alleviate these problems.

Another limitation of UniHOI is that it currently supports video reconstruction only for videos with an FPS above a certain threshold. This is due to its reliance on the off-the-shelf optical flow estimation module [83], which may perform poorly with sparse views. Integrating correspondence, matching, or optical flow prediction directly

into the model to enable fully end-to-end training could address this limitation [33, 74]. Sparse-view data also needs to be incorporated during training [77] to solve this problem.

Additionally, our model currently only supports a resolution of 288×384 . Training models at higher resolutions could enable more flexible applications. Our model also fails when the dynamic portion of the image is too large or contains too many moving objects beyond the ones being manipulated. Although we focus on egocentric HOI scenes, our training paradigm could be extended to more general cases. We plan to train this general scene model using motion mask priors derived from motion segmentation [10, 82], salient video segmentation [67], and semantic segmentation [28, 36]. We also encourage the community to propose more synthetic datasets [47, 95] to explore supervised learning approaches [77, 90].

K. Model Usage Guidance

Here, we briefly outline some practical guidance for UniHOI usage. We recommend users review these suggestions.

1. Video Scene: UniHOI achieves optimal performance with **indoor hand-object interaction videos** captured using a camera with a **non-extreme focal length**. While it is also capable for indoor static scenes, we highly recommend also trying models like DUS3R [77] or MAST3R [33], which are specifically trained for such tasks.

2. Video FPS: For stability, we recommend using **high FPS video** (≥ 15 FPS; higher FPS may be necessary for videos with large motion). While UniHOI can handle lower FPS videos, reconstruction quality may degrade if the optical flow module (GMFlow [83]) **struggles with sparse views**. For more details, see the GMFlow project².

3. Video Length: Our model can handle videos with an infinite number of frames at linear time complexity. However, using too many frames may lead to accumulated drift over time; **we recommend a limit of 100 frames**. When the model **returns to a previously visited viewpoint after a substantial viewpoint shift**, misalignment may appear in static regions due to the absence of loop closure detection functionality [43, 70] in current framework.

4. Inference Strategy: As shown in Appendix D, just set the window size to $N_w = 4$ and the window overlap to $N_o = 1$ to achieve the best performance and fastest inference speed.

²<https://github.com/haofeixu/gmflow>